Nano Research

ISSN 1998-0124 CN 11-5974/O4
https://doi.org/10.26599/NR.2026.94909108

Research Article

Bilayer hydrogel with ROS-triggered release and thermal regulation ability for diabetic infected wounds healing

Songjie Li[1], Han Chen[1], Xin Dan[1], Pu Yang[1], Yikun Ju[2], Tong Li[1], Yang Li[1](✉), Lanjie Lei[3](✉), Xing Fan[1](✉)

[1] Department of Plastic and Reconstructive Surgery, Xijing Hospital, Fourth Military Medical University, Xi'an 710032, China

[2] Department of Plastic and Aesthetic (Burn) Surgery, The Second Xiangya Hospital, Central South University, Changsha 410011, China

[3] Key Laboratory of Artificial Organs and Computational Medicine of Zhejiang Province, Shulan International Medical College, Institute of Translational Medicine, Zhejiang Shuren University, Hangzhou 310015, China

Nano Res., **Just Accepted Manuscript** • https://doi.org/10.26599/NR.2026.94909108

https://www.sciopen.com/journal/1998-0124 on Aug. 11, 2026

Just Accepted

TABLE OF CONTENTS (TOC)

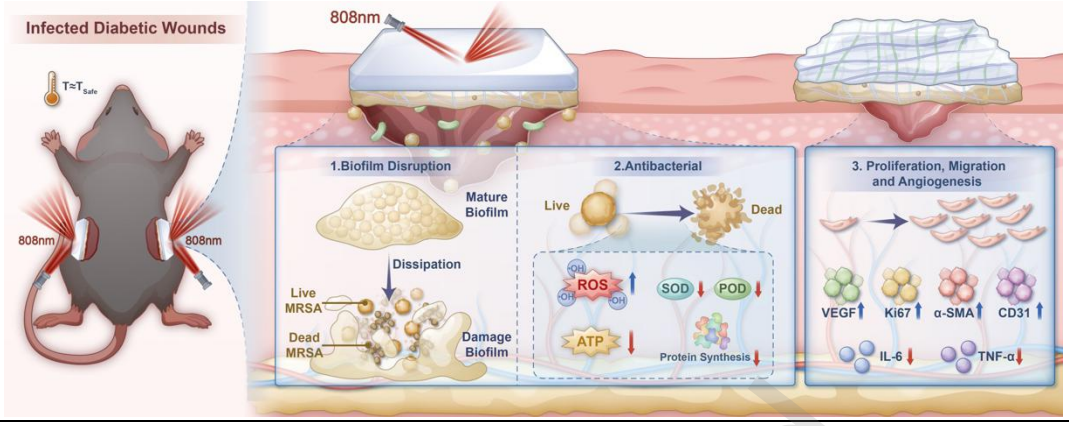

A reactive oxygen species-sensitive bilayer hydrogel exhibits antibacterial activity through self-regulated photothermal effects and promotes the healing of diabetic infected wounds.

Nano Research

Open Access

Research Article

Bilayer hydrogel with ROS-triggered release and thermal regulation ability for diabetic infected wounds healing

Songjie Li[1], Han Chen[1], Xin Dan[1], Pu Yang[1], Yikun Ju[2], Tong Li[1], Yang Li[1] ✉, Lanjie Lei[3] ✉, and Xing Fan[1] ✉

[1] *Department of Plastic and Reconstructive Surgery, Xijing Hospital, Fourth Military Medical University, Xi'an 710032, China*
[2] *Department of Plastic and Aesthetic (Burn) Surgery, The Second Xiangya Hospital, Central South University, Changsha 410011, China*
[3] *Key Laboratory of Artificial Organs and Computational Medicine of Zhejiang Province, Shulan International Medical College, Institute of Translational Medicine, Zhejiang Shuren University, Hangzhou 310015, China*

Received: 11 June 2026; **Revised:**5 August 2026; **Accepted:** 11 August 2026

✉Address correspondence to Xing Fan, fanxing@fmmu.edu.cn; Lanjie Lei, leilanjie1988@163.com; Yang Li, liyangzx@fmmu.edu.cn

Cite this article: *Nano Research*, 2026, 19, 94909108 https://doi.org/10.26599/NR.2026.94909108

ABSTRACT: Persistent bacterial infection, oxidative stress imbalance, and cellular dysfunction within diabetic wound microenvironments represent key clinical challenges that hinder wound healing. To address these challenges, we developed a smart reactive oxygen species (ROS)-responsive bilayer thermoregulatory hydrogel, PP@PZC&SAg. The system was based on a dynamically cross-linked phenylboronate ester network. The in situ green synthesis of Ag nanoparticles endowed the hydrogel with highly efficient photothermal bactericidal capabilities, whereas the incorporated Zn/Ce layered double oxide nanozyme (PZC) mimicked catalase activity to scavenge excess ROS in the microenvironment. The top layer comprised a thermosensitive hydrogel that utilized its phase-change properties to precisely regulate photothermal temperatures, thereby effectively destroying bacterial biofilms while preventing thermal damage to surrounding tissues. The PP@PZC&SAg hydrogel system exhibited considerable photothermal activity, rapidly reaching and maintaining a stable operating temperature while simultaneously eliminating bacteria and disrupting biofilms. Furthermore, through synergistic ROS scavenging and the release of active Zn and Ce ions, this system restored endothelial cell proliferation, migration, and tubulogenic capacity, which are typically impaired under high-glucose conditions, ultimately promoting rapid diabetic wound healing. This approach simultaneously combats bacterial infections, alleviates oxidative stress, and restores cellular function, thereby offering a novel, multifaceted, and targeted therapeutic strategy for treating diabetic wounds.

KEYWORDS: smart-responsive hydrogels, diabetic infected wounds, tissue repair, nanoparticles, photothermal therapy

1 Introduction

Diabetes causes chronic, hard-to-heal wounds that represent a substantial global public health concern [1–4]. The underlying pathophysiological mechanisms are complex and include sustained oxidative stress induced by a hyperglycemic microenvironment, excessive inflammatory responses, impaired microvascular neogenesis, and persistent bacterial biofilm infections [5–8], thereby affecting the normal healing of the wound. Although various treatment methods, such as skin grafting, are used clinically, challenges such as bacterial infection and severe oxidative stress remain difficult to effectively address [9]. Recently, hydrogel dressings have demonstrated outstanding therapeutic efficacy in treating diabetic wounds [10–12]. Specially modified hydrogels, or those supplemented with bioactive components, can effectively ameliorate the pathological microenvironment at wound sites [13–15]. However, these strategies are largely reactive and symptomatic, lacking the ability to proactively and coordinately regulate the infection- and oxidative stress-associated microenvironment. Therefore, a new generation of smart dressing systems that simultaneously address multiple pathological conditions is urgently needed.

Among the various strategies for combating infections, photothermal therapy (PTT) using Ag nanoparticles has demonstrated considerable potential owing to its broad-spectrum efficacy, high efficiency, and low risk of resistance development [16, 17]. However, the risk of biological toxicity associated with traditionally synthesized Ag nanoparticles limits their clinical application. Furthermore, in the absence of temperature control during PTT, the excessive heat generated by Ag is highly likely to cause irreversible thermal damage to surrounding healthy tissues [18]. Therefore, identifying an environmentally friendly strategy for Ag synthesis and incorporating an intelligent temperature-control mechanism are key prerequisites for achieving safe and efficient photothermal antibacterial activity. In this study, PZC was prepared based on Zn/Ce-layered double oxide (ZnCe-LDO) nanozymes with pro-angiogenic and valence-cycling antioxidant functions [19–22]. However, the effective integration of these functional components and their precise delivery remain major constraints for achieving rapid

diabetic wound healing. Reactive oxygen species (ROS)-responsive hydrogels undergo specific cleavage in the high-concentration H_2O_2 environment of diabetic wounds; the collapse of the hydrogel network enables controlled nanoparticle (NP) delivery, thereby facilitating sustained and slow release. In addition, we introduced lower critical solution temperature (LCST) thermoresponsive polymers to address the clinical challenge of uncontrolled temperature increases during PTT [23].

Here, we developed a novel hydrogel, PP@PZC&SAg, for treating diabetic wounds. PP@PZC&SAg integrates the in situ green synthesis of Ag, nanozyme-mediated antioxidant activity, and a bilayer intelligent temperature-control system (Fig. 1). The system uses an innovative two-layer integrated structure, with the lower layer comprising a ROS-responsive, self-healing hydrogel (PCS hydrogel) formed by cross-linking chitosan modified with 3-carboxyphenylboronic acid (CSPBA) and polyvinyl alcohol (PVA) via phenylboronate ester bonds. The lower layer incorporates PZC and utilizes silk protein for the in situ green synthesis of Ag, achieving on-demand, triggered release of Ag and PZC in response to elevated H_2O_2 concentrations at the wound site [24–26]. The upper layer consists of a temperature-sensitive hydrogel, P(NIPAM-AM), which exhibits LCST properties [27]. This bilayer structure endows the system with unique self-regulating photothermal response properties. Upon exposure to near-infrared light, the underlying Ag layer rapidly generates heat to kill bacteria. When the temperature exceeds a preset safety threshold, the P(NIPAM-AM) gel undergoes a phase transition and becomes opaque, physically blocking further light penetration and thereby maintaining the wound temperature within a biologically safe range. The results demonstrated that PP@PZC&SAg significantly accelerated diabetic wound healing through ROS scavenging, photothermal antibacterial effects, and angiogenesis induction. This innovative strategy is expected to advance clinical diabetic wound management and holds substantial research and translational value.

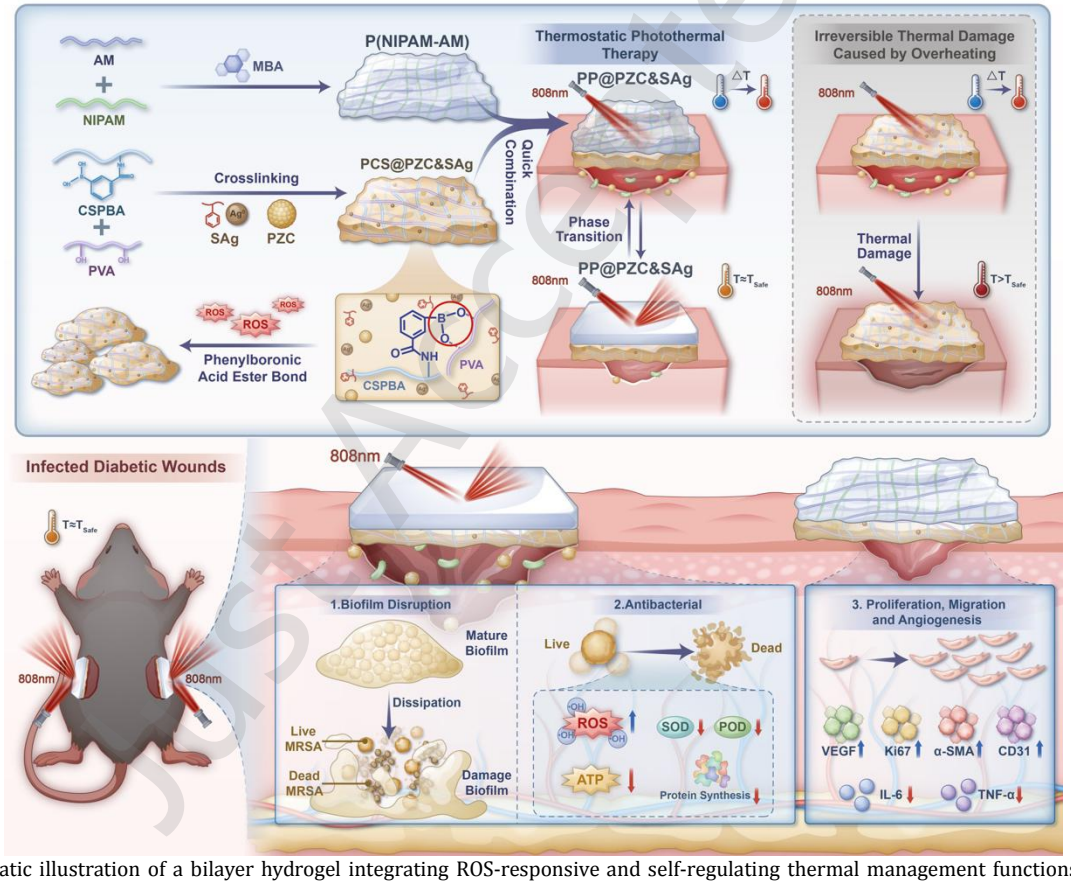

Figure 1 Schematic illustration of a bilayer hydrogel integrating ROS-responsive and self-regulating thermal management functions to promote the healing of diabetic infected wounds.

2 Results and discussion

2.1 Ag and PZC characterization

Given the susceptibility of diabetic wounds to bacterial infection and severe oxidative stress, we developed a dual-NP system comprising Ag and PZC to exert antibacterial and antioxidant effects (Fig. 2(a) and 2(b)). Ultraviolet (UV)–visible spectroscopy revealed that the synthesized Ag exhibited an evident absorption peak at approximately 420 nm, clearly distinguishing it from $AgNO_3$ and sericin solution (SS), thereby indicating successful Ag nanoparticle synthesis (Fig. S1(a) in the Electronic Supplementary Material (ESM)). X-ray diffraction (XRD) patterns confirmed the face-centered cubic structure of Ag (Fig. 2(c)). X-ray photoelectron spectroscopy (XPS) and high-resolution XPS spectra of the Ag 3d core level confirmed the presence of the Ag elemental signal (Fig. 2(d) and 2(e)). Zeta potential analysis confirmed the colloidal stability of Ag (Fig. S1(b) in the ESM). Transmission electron microscopy (TEM) results indicated that the average size of Ag particles was approximately 24 nm (Fig. 2(g) and 2(k)). TEM was also

used to verify the uniform distribution of Ag within the composite hydrogel (Fig. 2(k)). To assess the biocompatibility of in situ-synthesized Ag, we conducted preliminary Cell Counting Kit-8 proliferation assays, the results of which indicated that Ag exhibited high cellular compatibility (Fig. S1(c) in the ESM). We then verified the relevant performance characteristics of PZC. The XRD results showed diffraction peaks corresponding to CeO_2 and ZnO, confirming the successful synthesis of the ZnCe-LDO nanozyme (Fig. 2(f)). The XPS results, TEM images, and elemental mapping further confirmed the presence of Zn and Ce (Fig. 2(h), 2(i), 2(j), and 2(l)). Zeta potential analysis showed that the zeta potential of PZC exhibited a unimodal distribution (Fig. S4(a) in the ESM). Experimental results of catalase-like activity indicated that the enzymatic activity of PZC increased in a concentration-dependent manner and effectively decomposed H_2O_2 into H_2O and O_2 (Fig. S1(d) in the ESM).

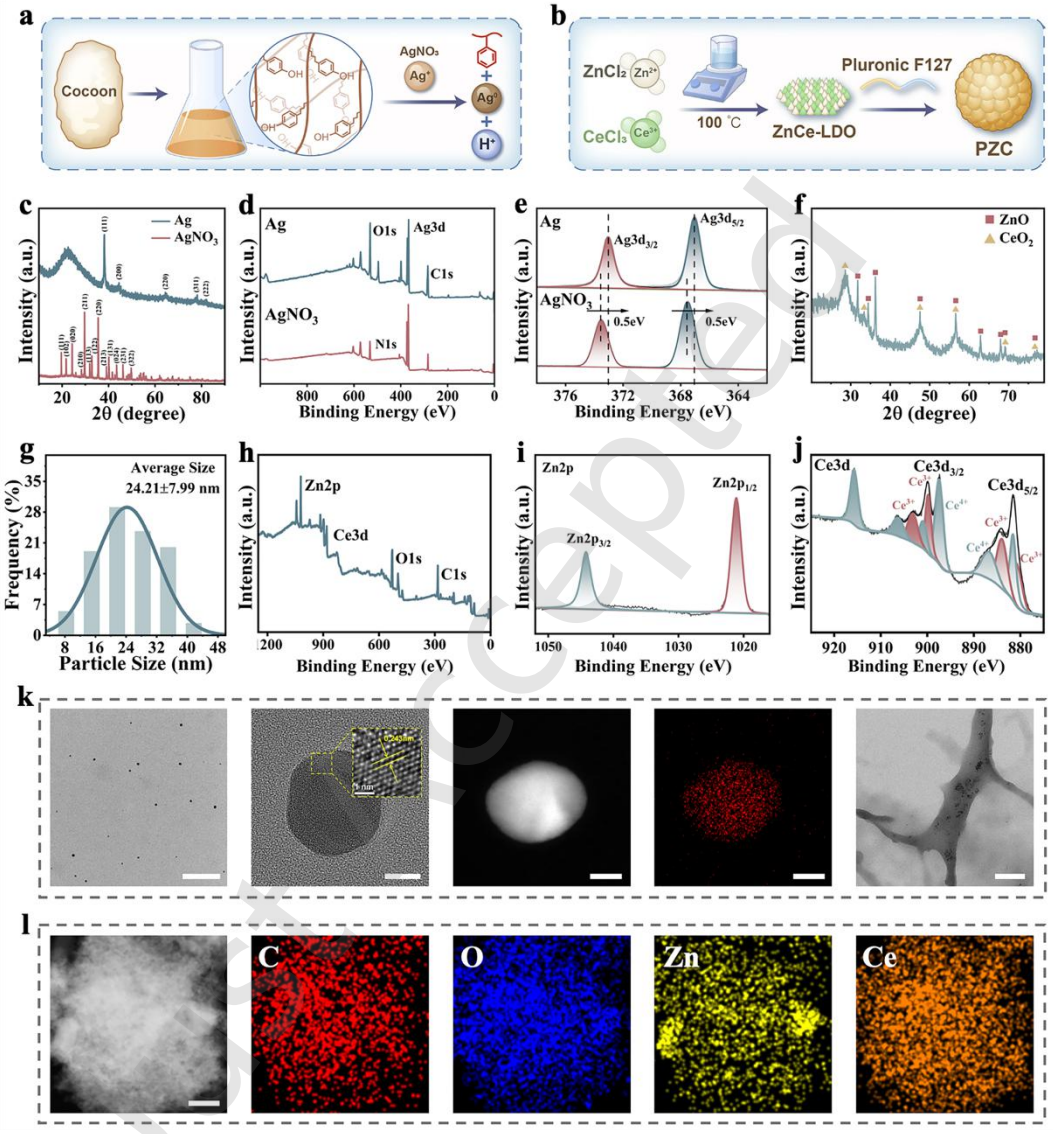

Figure 2 Characterization of Ag and PZC. (a) Schematic of Ag synthesis. (b) Schematic of PZC synthesis. (c) XRD pattern of Ag. (d) XPS spectrum of Ag. (e) High-resolution XPS spectrum of the Ag 3d core level. (f) XRD pattern of PZC. (g) Particle size analysis of Ag. (h) XPS spectrum of PZC. (i) High-resolution XPS spectrum of the Zn 2p core level. (j) High-resolution XPS spectrum of the Ce 3d core level. (k) TEM analysis of Ag (scale bars: 500, 10, 10, 10, and 200 nm). (l) TEM analysis of PZC (scale bar: 100 nm).

2.2 Characterization of composite hydrogels

Standalone NP use presents issues such as uncontrolled drug release and susceptibility to degradation; therefore, we developed a bilayer hydrogel as a carrier to enhance the efficacy of Ag and PZC. The PCS hydrogel incorporating SAg and PZC was used as the lower layer (PCS@PZC&SAg), and P(NIPAM-AM) served as the upper layer. The two gels adhered to each other to form a PP bilayer hydrogel (PP@PZC&SAg). The pore structure of the hydrogel was observed using scanning electron microscopy (SEM) (Fig. 3(a)). Both layers exhibited highly porous structures, which provided favorable conditions for NP encapsulation and precise delivery. Elemental mapping indicated that SAg and PZC were uniformly distributed within the PCS hydrogel (Fig. S2 in the ESM). The hydrogels were further evaluated using rheological testing. The time-scan rheological test results indicated that the hydrogel modulus of the PP@PZC&SAg lay between those of PCS@PZC&SAg and P(NIPAM-AM) (Fig. S3(a) in the ESM). Amplitude scanning further confirmed the stability and ability of the hydrogel to fully adapt to skin wound movement (Fig. 3(b)). Angular frequency scanning experiments indicated that the hydrogel did not fracture

within the 0–80 rad/s range, demonstrating good viscoelasticity (Fig. 3(c)). Additionally, we conducted cyclic stress tests, the results of which showed that all three hydrogels were capable of undergoing spontaneous structural transformations in response to alternating high and low strains, demonstrating good self-healing properties (Fig. 3(d) and Fig. S3(b) and S3(c) in the ESM). In addition, the thermosensitive properties of the P(NIPAM-AM) hydrogel were macroscopically verified. As shown in Fig. 3(e) and Fig. S1(e) in the ESM, P(NIPAM-AM) gels were transparent masses at room temperature. Upon heating, the gel dehydrated and transformed into an opaque white solid. As the temperature naturally decreased, the hydrogel absorbed water and gradually returned to its transparent state, indicating that the process was reversible. Successful PCS hydrogel preparation was confirmed by Fourier transform infrared spectroscopy (FTIR) (Fig. S3(d) in the ESM). The C=O (amide I) stretching vibration produced an absorption peak at 1641 cm^{-1}. However, the absorption bands at 1324 and 707 cm^{-1} were attributed to boronic acid and benzene ring vibrations, respectively. The ^{1}H-NMR spectrum further confirmed the chemical structure of PCS (Fig. S3(e) and S3(f) in the ESM). Comparison with the ^{1}H-NMR spectrum of CS revealed that PCS exhibited distinct peaks at 7.4–8.3 ppm, which were associated with aromatic protons. These results confirmed the successful grafting of 3-carboxybenzeneboronic acid (PBA-COOH). The ROS-responsive properties of the PCS hydrogels were further verified (Fig. 3(f)). In the presence of H_2O_2, the hydrogel transformed from a solid to a fluid state. This behavior was attributed to the dynamic nature of phenylboronate bonds under the influence of ROS, which led to the gradual collapse of the hydrogel network. We conducted further analysis of PCS hydrogel degradation in the presence of H_2O_2 (Fig. S4(b) in the ESM). The results showed that, compared with the PBS environment, H_2O_2 promoted the rapid degradation of PCS hydrogels. At the same time, the cumulative release of metal ions from the hydrogel confirmed that, in the presence of H_2O_2, the cumulative release was significantly higher than that in the PBS group (Fig. S4(c)-S4(e) in the ESM). These findings collectively confirmed the ROS-responsive properties of PCS hydrogels, which were capable of degrading in the high-ROS environment of diabetic wounds, thereby enabling stable release of the loaded drug. We then verified the photothermal effect of the composite hydrogel. Under irradiation with near-infrared light at 808 nm, PCS@PZC&SAg exhibited a thermal generation capacity that increased with increasing laser intensity and Ag concentration, with a maximum photothermal equilibrium temperature of 88 °C (Fig. 3(g) and Fig. S5 in the ESM). After five repeated exposures to near-infrared light, PCS@PZC&SAg continued to exhibit stable photothermal effects, with no significant change in its heat-generating performance (Fig. 3(m)). To overcome the drawbacks of traditional materials, which tend to overheat and cause thermal damage to wound sites, we introduced an LCST-type thermoresponsive polymer (Fig. 3(j)). We then constructed the P(NIPAM-AM) hydrogel to investigate its effect on the photothermal properties of PCS@PZC&SAg. P(NIPAM-AM) is a copolymer of the hydrophilic monomers acrylamide (AM) and N-isopropylacrylamide (NIPAM). Its phase transition temperature depends on the ratio of NIPAM to AM. As shown in Fig. 3(h) and 3(k), when coated with P(NIPAM-AM) (NIPAM:AM = 10:1), the maximum photothermal temperature of the PP@PZC&SAg stabilized at approximately 48.5 °C. Although this temperature exceeds the conventional safety threshold for static tissue (approximately 42–45 °C), thermal damage is determined by the cumulative heat dose rather than by the temperature itself. At the *in vivo* 5-minute exposure time used in this study, the cumulative heat dose was well below the threshold for irreversible tissue damage. Furthermore, multiple studies have reported that the 48–50 °C range is a safe and effective therapeutic window for photothermal antimicrobial treatment when applied for short durations (≤10 min). For example, Fu et al. [28] developed a temperature-sensitive hydrogel-based constant-temperature photothermal therapy system that achieved enhanced healing of bacterial-infected wounds at approximately 49 °C without causing significant thermal damage to healthy tissue. Similarly, Zhang et al. [29] developed a temperature-sensitive chitosan hydrogel that exhibited broad-spectrum antibacterial and anti-biofilm effects at a moderate temperature (~48 °C). These studies collectively support the use of 48.5 °C as a safe temperature for short-term photothermal antimicrobial therapy. Compared with PCS@PZC&SAg, the PP@PZC&SAg enabled precise and effective temperature regulation. Two additional P(NIPAM-AM) hydrogels with different ratios (NIPAM:AM = 30:1 and 50:1) also demonstrated effective temperature regulation, with equilibrium temperatures of approximately 43.3 °C and 37.4 °C, respectively (Fig. 3(l), 3(n), and 3(o)). At the same time, we conducted rheological tests on the gelation and self-healing properties of hydrogels prepared using these two ratios. The results showed that both exhibited good gelation and self-healing capabilities (Fig. S6 in the ESM). To ensure safety while achieving an effective antimicrobial range, the 10:1 ratio was selected for subsequent experiments. Fig. 3(k) illustrates the color change of P(NIPAM-AM) during the heating process. As the temperature increased, owing to the photothermal effect of PCS@PZC&SAg, P(NIPAM-AM) underwent a phase transition from a transparent to an opaque white state, thereby blocking near-infrared light transmission and achieving temperature regulation. Additionally, we measured the transmittance of P(NIPAM-AM) under an 808 nm laser at different temperatures. The results were consistent with those shown in Fig. 3(k), with the phase transition temperature corresponding to 5% transmittance occurring at approximately 48.5 °C (Fig. 3(i)). To further verify the stability of P(NIPAM-AM)'s temperature-control capabilities, we subjected the PP@PZC&SAg to five photothermal cycles. The results showed that the photothermal and temperature-control capabilities of the PP@PZC&SAg remained unaffected (Fig. S4(f) in the ESM).

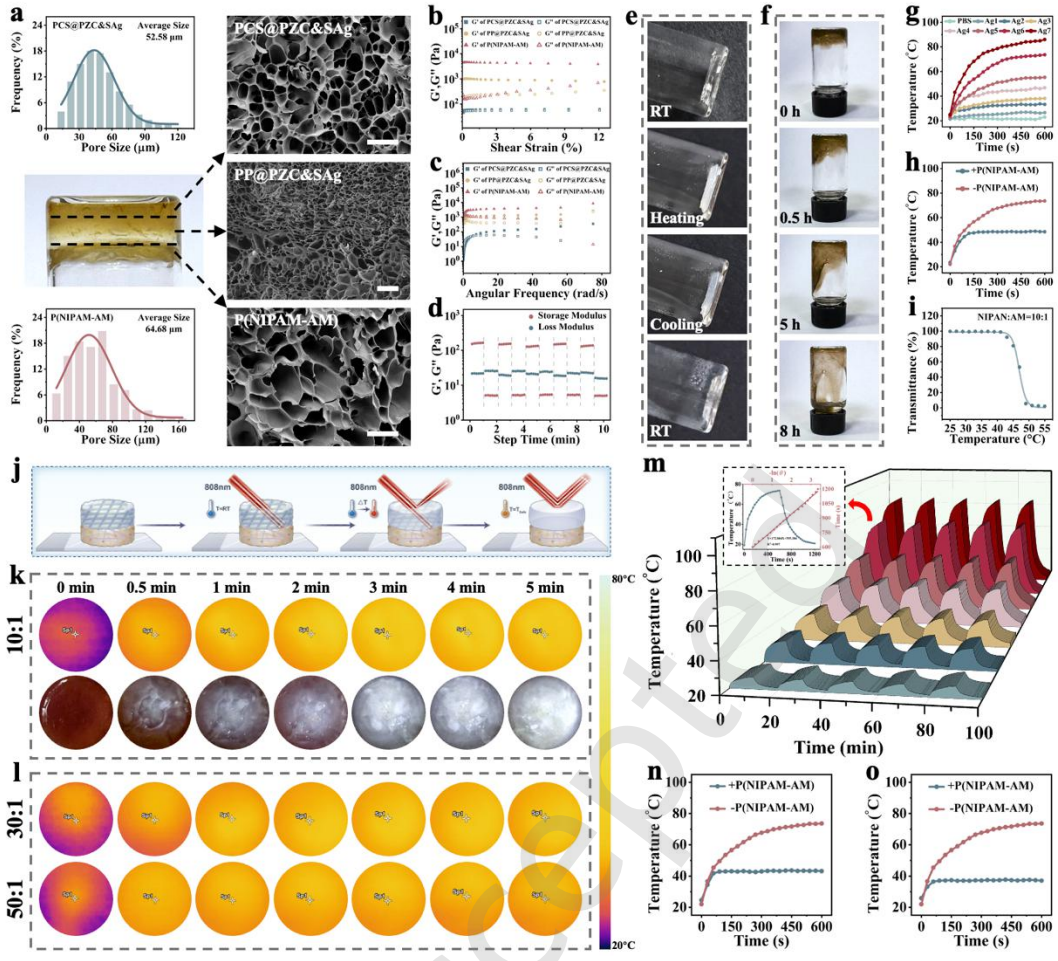

Figure 3 Characterization of composite hydrogels. (a) SEM analysis of the composite hydrogel (scale bars: 100, 200, and 100 μm). (b) Rheological behavior under amplitude scanning. (c) Angular-frequency sweep of the hydrogels. (d) Rheological properties when the alternating step strain was switched from low to high. (e) Thermosensitive properties of P(NIPAM-AM). (f) ROS response characteristics of PCS. (g) Photothermal effect of PCS@PZC&SAg at different concentrations. (h) Temperature-regulating properties of PP@PZC&SAg. (i) Light transmittance of P(NIPAM-AM) at different temperatures. (j) Schematic diagram illustrating the principle of PP@PZC&SAg automatic temperature control. (k) Temperature and morphological changes in PP@PZC&SAg (10:1) within 5 min of exposure to light. (l) Temperature changes in PP@PZC&SAg (30:1 and 50:1) within 5 min of exposure to light. (m) Photothermal cycling performance of the PCS@PZC&SAg. (n) Temperature changes in PP@PZC&SAg (30:1) following exposure to light. (o) Temperature changes in PP@PZC&SAg (50:1) following illumination.

2.3 *In vitro* antimicrobial activity and potential mechanisms

Bacterial infections are common in diabetic wounds and can disrupt the wound microenvironment and hinder healing. We evaluated the antimicrobial properties of the hydrogel using *Escherichia coli* (*E. coli*) and methicillin-resistant *Staphylococcus aureus* (MRSA). As shown in Fig. 4(a), the presence or absence of near-infrared irradiation in the control group did not significantly affect bacterial counts. The PP@PZC&SAg complex significantly reduced the number of *E. coli* cells; however, its antibacterial activity against MRSA was limited. Following treatment with near-infrared light, the PP@PZC&SAg+L group exhibited antibacterial activity against *E. coli* and MRSA exceeding 95% (Fig. 4(d) and 4(e)). The antimicrobial activities of the hydrogels were further validated using the Alamar Blue assay, with the PP@PZC&SAg+L group demonstrating the highest antimicrobial efficacy (Fig. 4(f) and 4(g)). We examined morphological changes in bacteria following treatment with different groups using SEM (Fig. 4(b)). Following hydrogel treatment, bacteria exhibited varying degrees of shrinkage and surface disruption, with compromised membrane integrity. Cytoplasmic leakage analysis showed significant leakage of β-galactosidase and intracellular proteins, which was associated with membrane disruption caused by hydrogel treatment (Fig. 4(h), 4(i), and S7 in the ESM). We used TEM to further examine the effects of the hydrogel on the internal structures and membrane architectures of bacteria. In the control group, both bacteria exhibited normal morphology, with some bacteria undergoing division. Following treatment with PP@PZC&SAg+L, bacterial membrane structures were disrupted, resulting in cytoplasmic leakage (Fig. 4(j)). In addition, we assessed the ability of the hydrogel to disrupt bacterial biofilms using crystal violet and live/dead staining. Crystal violet staining indicated that bacterial biofilm formation decreased following treatment with PP@PZC&SAg+L, accompanied by a corresponding decrease in absorbance at 570 nm (Fig. 4(c) and 4(k)). The live/dead staining results were consistent with these findings. The PP@PZC&SAg+L group exhibited extensive red fluorescence in bacterial cells, indicating extensive bacterial death

associated with biofilm disruption (Fig. 4(l) and S8 in the ESM). We then separated the components of the composite hydrogel to analyze the antimicrobial efficacy of each component individually. The results of the bacterial plate spread tests, live/dead staining, and SEM analyses were consistent, all showing that the PCS hydrogel, PZC, SAg, and SAg+L exhibited relatively pronounced antimicrobial activity, with SAg+L demonstrating the strongest antimicrobial effect (Fig. S9 in the ESM).

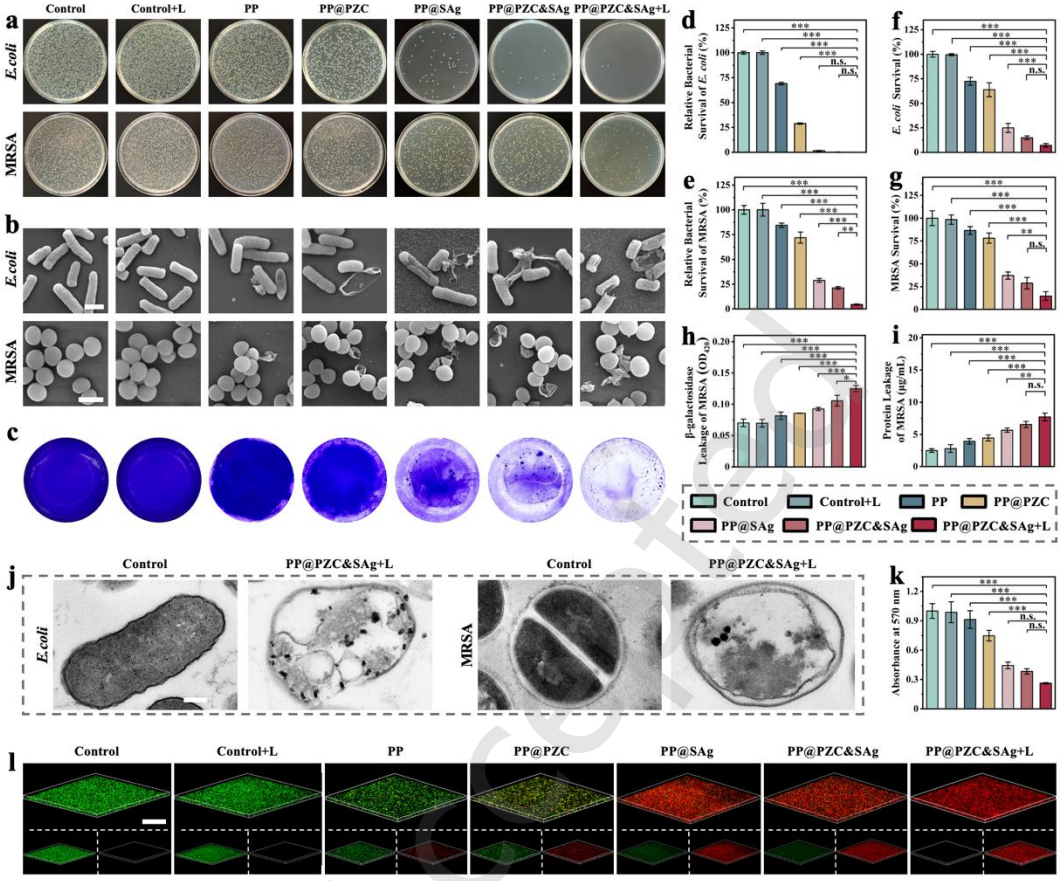

Figure 4 *In vitro* antimicrobial activity. (a) Bacterial plate count test. (b) SEM observations of bacterial morphology (scale bar: 1 μm). (c) Crystal violet staining of bacterial biofilms. (d) Quantitative analysis of *E. coli* plate counts. (e) Quantitative analysis of MRSA plate cultures. (f) Analysis of *E. coli* survival rates. (g) Analysis of MRSA survival rates. (h) β-Galactosidase leakage in MRSA. (i) Protein leakage in MRSA. (j) TEM observation of ultrastructural and membrane damage in *E. coli* and MRSA (scale bar: 200 nm). (k) Quantitative analysis of biofilm staining with crystal violet. (l) Live/dead staining of bacterial biofilms (scale bar: 200 μm).

We used a 2′,7′-dichlorodihydrofluorescein diacetate (DCFH-DA) probe to assess oxidative stress levels in bacteria. As shown in Fig. 5(a), fluorescence intensity increased significantly following hydrogel treatment, with the PP@PZC&SAg+L group showing the most pronounced effects, indicating a sharp increase in intracellular ROS levels (Fig. 5(b) and 5(c)). The effect of hydrogel treatment on bacterial ATPase activity was further investigated, and the results revealed reduced enzyme activity accompanied by inhibited ATP production (Fig. 5(d) and S10(a) in the ESM). Furthermore, we observed decreased protein levels within bacteria, indicating protein synthesis inhibition, which may be linked to reduced ATP production and an increased oxidative stress environment within bacteria (Fig. 5(e) and S10(b) in the ESM). Bacterial membrane potential was measured, and the results showed that the membrane potential decreased following hydrogel treatment, indicating damage to bacterial membrane structures (Fig. 5(f) and S10(c) in the ESM). As ROS fluorescence analysis indicated that bacteria were under high oxidative stress following hydrogel treatment, we further investigated changes in the activity of redox-related enzymes within bacteria. Superoxide dismutase (SOD) and peroxidase (POD) activities within bacteria decreased following hydrogel treatment, thereby reducing the capacity of bacteria to scavenge free radicals and exacerbating oxidative stress (Fig. 5(g), 5(h), S10(d) in the ESM, and S10(e) in the ESM). The antioxidant glutathione (GSH) was then added to evaluate bacterial survival. Compared with the control group without GSH, the antioxidant effect of GSH counteracted the antibacterial effect of the hydrogel, resulting in improved bacterial survival (Fig. 5(i) and S10(f) in the ESM). This finding provides further evidence that hydrogels exhibit antibacterial activity by increasing oxidative stress levels within bacteria.

To elucidate the antimicrobial mechanism, we performed RNA sequencing analysis of MRSA treated with PP@PZC&SAg+L. As shown in Fig. 5(j) and 5(k), the treatment group exhibited upregulation of 429 genes and downregulation of 478 genes. Analysis of Kyoto Encyclopedia of Genes and Genomes (KEGG) annotations for these differentially expressed genes (DEGs) revealed that the hydrogel affected bacterial nucleotide, amino acid, and carbohydrate metabolism, as well as signal transduction and

membrane transport (Fig. 5(l)). We then used a heatmap to illustrate the expression patterns of relevant genes, revealing that PP@PZC&SAg+L treatment affected the expression of genes associated with ATP synthesis and enzyme metabolism within bacteria (Fig. 5(m)). The results of Gene Ontology (GO) enrichment analysis further indicated that nucleotide biosynthesis, protein synthesis, processing, and metabolism were affected in the treatment group, along with alterations in oxidoreductase activity, compared with those in the control group (Fig. 5(n)). These findings further confirmed that hydrogel treatment affected bacterial biosynthesis and energy metabolism, ultimately leading to bacterial death and inhibited proliferation.

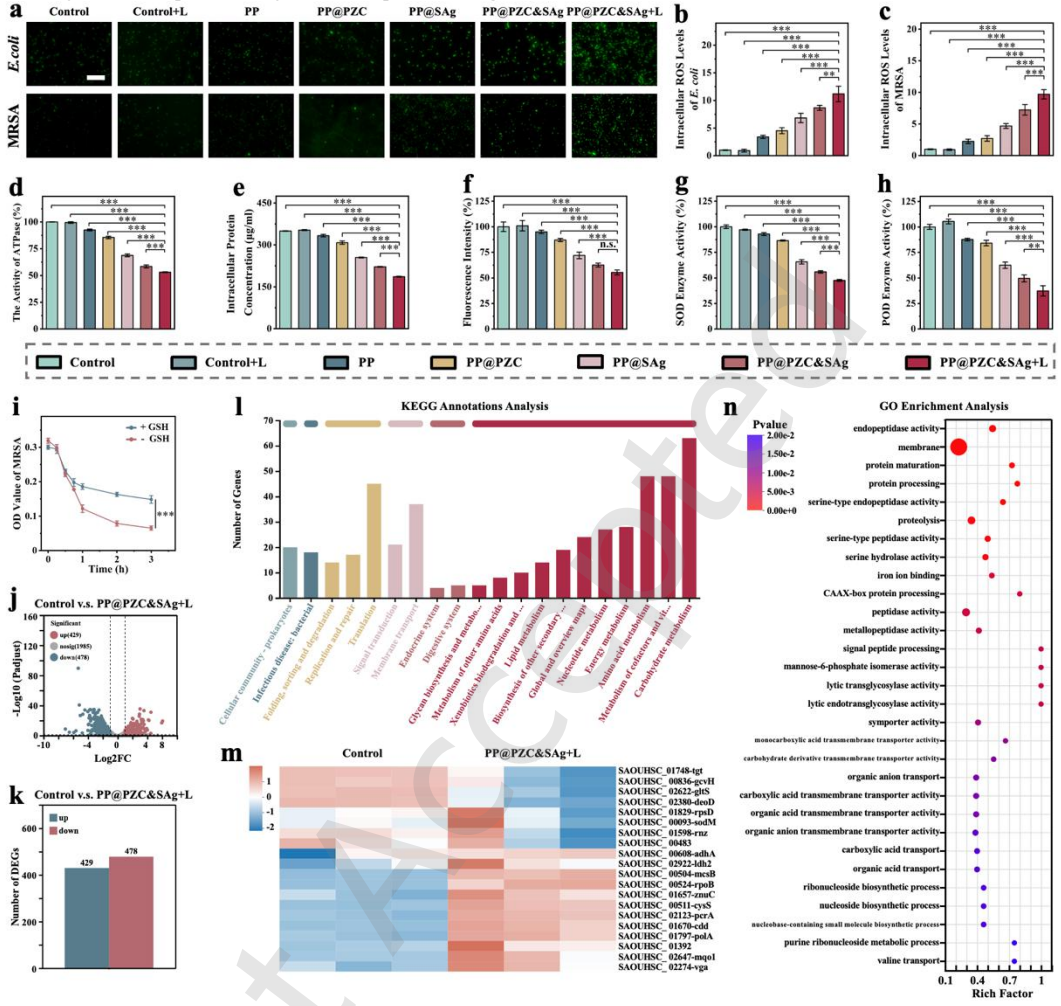

Figure 5 Antimicrobial properties of hydrogels. (a) Fluorescent staining of ROS levels within bacteria (scale bar: 50 μm). (b) Quantitative analysis of ROS levels in *E. coli*. (c) Quantitative analysis of ROS levels in MRSA. (d) Analysis of ATPase activity in MRSA. (e) Protein production within MRSA. (f) Analysis of membrane potential levels in MRSA. (g) SOD enzyme activity in MRSA. (h) POD activity in MRSA. (i) Bacterial relative survival rates with and without GSH. (j) Volcano plot of DEGs. (k) Number of DEGs. (l) KEGG annotation analysis. (m) Heatmap of bacterial DEGs. (n) GO enrichment analysis of DEGs.

2.4 Composite hydrogels improve cell function in high-glucose environments

The hyperglycemic state associated with diabetic wounds elevates intracellular ROS levels, impairs cellular functions such as proliferation and migration, and inhibits the tubulogenic capacity of human umbilical vein endothelial cells (HUVECs). PP@PZC&SAg promotes cell function, which is inhibited by high glucose levels, by modulating cellular oxidative stress levels. First, we assessed the biocompatibility of the hydrogels using experimental assays. The hydrogel functioned without affecting cell viability (Fig. 6(a) and Fig. S11(a) and S11(b) in the ESM). We then performed a Ki67 immunofluorescence assay to assess the extent to which the hydrogel improved cell proliferation (Fig. 6(b)). The results revealed that cell proliferation was significantly inhibited by HG treatment. In contrast, fluorescence intensity in the HG+PP@PZC&SAg group was significantly enhanced, suggesting partial restoration of proliferation. We further validated these findings using a 5-vinyl-2′-deoxyuridine (EdU) cell proliferation assay (Fig. 6(f) and 6(g)). The number of cells in the proliferation phase in the HG+PP@PZC&SAg group was comparable to that in the control group. This finding indicates that the introduction of PP@PZC&SAg effectively enhanced cellular growth in the HG environment.

Subsequently, we validated the effect of the hydrogel on cell migration from different perspectives using Transwell migration and cell scratch assays. The number of cells migrating through the Transwell and the scratch closure rate were significantly improved in the HG+PP@PZC&SAg group (Fig. 6(c), S11(c) in the ESM, and S12 in the ESM). Additionally, we assessed the tubule-forming capacity of

HUVECs using Matrigel tube formation assays and vascular endothelial growth factor (VEGF) immunofluorescence staining (Fig. 6(d), 6(e), and S11(d) in the ESM). Hydrogel treatment promoted the formation of more extensive tubular networks *in vitro*, which may support neovascularization at the wound site, thereby enhancing oxygen delivery and nutrient exchange and promoting wound healing. To further investigate the effects of individual components in the composite hydrogel on cell behavior, we separated the components and conducted scratch and tube formation assays on each component individually (Fig. S13 in the ESM). It can be observed that, in the HG environment, the abilities of cells to migrate and form tubules are significantly inhibited. Interventions involving each component had a promoting effect on both cell migration and tubule formation. The functional improvement in cells was most pronounced following PZC treatment, which was attributable to PZC's potent antioxidant properties.

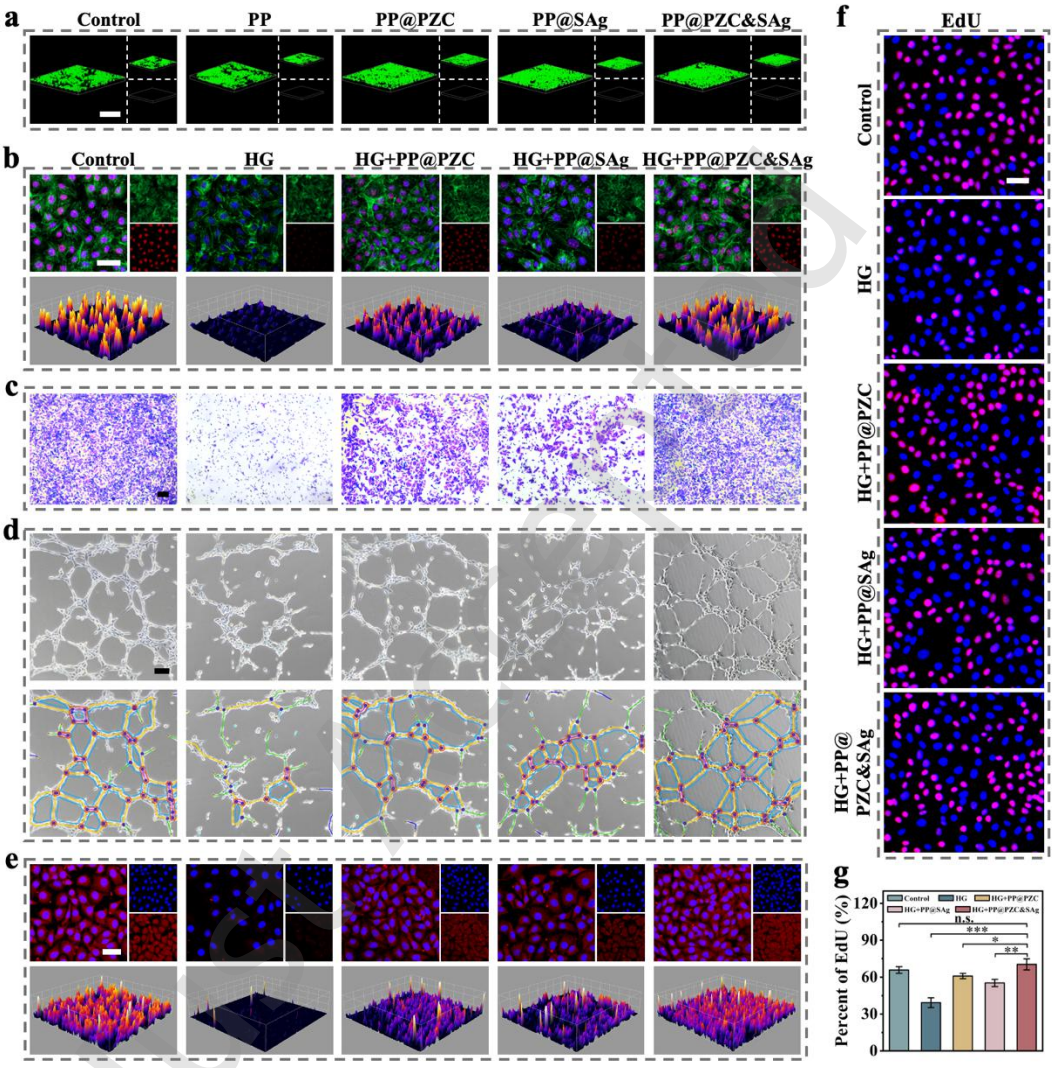

Figure 6 Composite hydrogels improve cell function in high-glucose environments. (a) Cell live/dead staining (scale bar: 200 μm). (b) Ki67 cell immunofluorescence staining (scale bar: 50 μm). (c) Transwell assay to verify cellular migration capacity (scale bar: 100 μm). (d) HUVEC tube formation assay (scale bar: 100 μm). (e) VEGF cell immunofluorescence staining (scale bar: 50 μm). (f) EdU proliferation assay (scale bar: 100 μm) and quantitative analysis (g).

2.5 Composite hydrogels promote infected diabetic wound healing

The PP@PZC&SAg hydrogel demonstrated outstanding efficacy in terms of antimicrobial activity and cellular function improvement. We further investigated the effects of these hydrogels on MRSA-infected diabetic wounds using a full-thickness skin defect model. *In vitro* degradation experiments on the hydrogel, together with macroscopic observations from *in vivo* experiments, indicated that it degraded slowly over time and was almost completely degraded by day 12. Wound healing was accelerated following hydrogel treatment, and by day 12, the wound area was significantly reduced (Fig. 7(a)). The PP@PZC&SAg+L group exhibited the most pronounced wound-healing ability (Fig. 7(d)). Fig. 7(b) shows the temperature changes in the control and PP@PZC&SAg+L groups during 5 min of near-infrared irradiation. The wound temperature in the PP@PZC&SAg+L group increased rapidly and stabilized at approximately 48.5 °C. Within a 5-min irradiation period, 48.5 °C represented a safe treatment temperature that ensured effective sterilization without causing significant thermal damage to surrounding tissues. Observations of the wounds and surrounding tissues in mice during the experiment revealed no obvious signs of burns,

further confirming the safety of this treatment regimen. Bacterial plate counts showed that a large number of bacteria remained in the control group, whereas bacterial counts were significantly reduced in the hydrogel-treated groups, with further reductions after exposure to light (Fig. 7(c) and 7(g)). We collected samples from the wound and surrounding areas and performed Giemsa and Gram staining to assess the presence of bacterial infection at the wound site. Bacterial counts were significantly reduced in the PP@PZC&SAg+L group (Fig. 7(f) and 7(i)). Gram staining revealed pronounced purple coloration in the control group, indicating significant bacterial infection, which was markedly reduced following hydrogel treatment (Fig. S16(a) in the ESM). Collectively, these findings demonstrated the effectiveness of hydrogel treatment in alleviating wound infections, thereby laying the groundwork for rapid wound healing. Finally, we collected tissue samples from the wound and performed histological analysis. The results of hematoxylin and eosin (H&E) staining were consistent with the macroscopic healing findings; the narrowest granulation tissue width was observed in the PP@PZC&SAg+L group, indicating enhanced wound healing (Fig. 7(e) and 7(h)). To further evaluate the *in vivo* therapeutic efficacy of the composite hydrogel in diabetic infected wounds, we incorporated antibiotics and hydrogel dressings as comparative benchmarks for in-depth assessment. The results showed that, compared with the control group, all three treatment groups demonstrated beneficial effects in promoting wound healing. Among these, PP@PZC&SAg+L had the strongest effect on promoting re-epithelialization (Fig. S14 in the ESM).

We then analyzed the wound sites in the control and PP@PZC&SAg+L treatment groups using transcriptomic sequencing. Sequencing results revealed differences in gene expression between the two groups, including 1,547 upregulated and 2,882 downregulated genes, respectively (Fig. 7(j) and 7(k)). The heatmap illustrates the expression levels of specific genes (Fig. 7(l)). Gene expression levels associated with proliferation, healing, and skin development were elevated in the treatment group. In contrast, the expression of oxidative stress-related genes, such as interleukin-6 (IL-6), MMP9, and IL-1β, was reduced in the treatment group. KEGG enrichment analysis revealed that DEGs were significantly enriched in the *S. aureus* infection pathway (Fig. 7(m)). Gene set enrichment analysis also indicated that this pathway was activated in the control group, further confirming the effective ability of the treatment group to clear bacteria from the wound site (Fig. S15 in the ESM). Furthermore, KEGG enrichment analysis revealed enrichment of pathways such as PI3K-Akt, JAK-STAT, tumor necrosis factor (TNF), NF-κB, NOD-like receptors, and TGF-β, indicating that the hydrogel exerted antioxidant, anti-inflammatory, and wound-healing effects on the wound surface (Fig. 7(m)). GO enrichment analysis was consistent with the above results, providing further evidence for the wound-healing effects of the hydrogel (Fig. 7(n)).

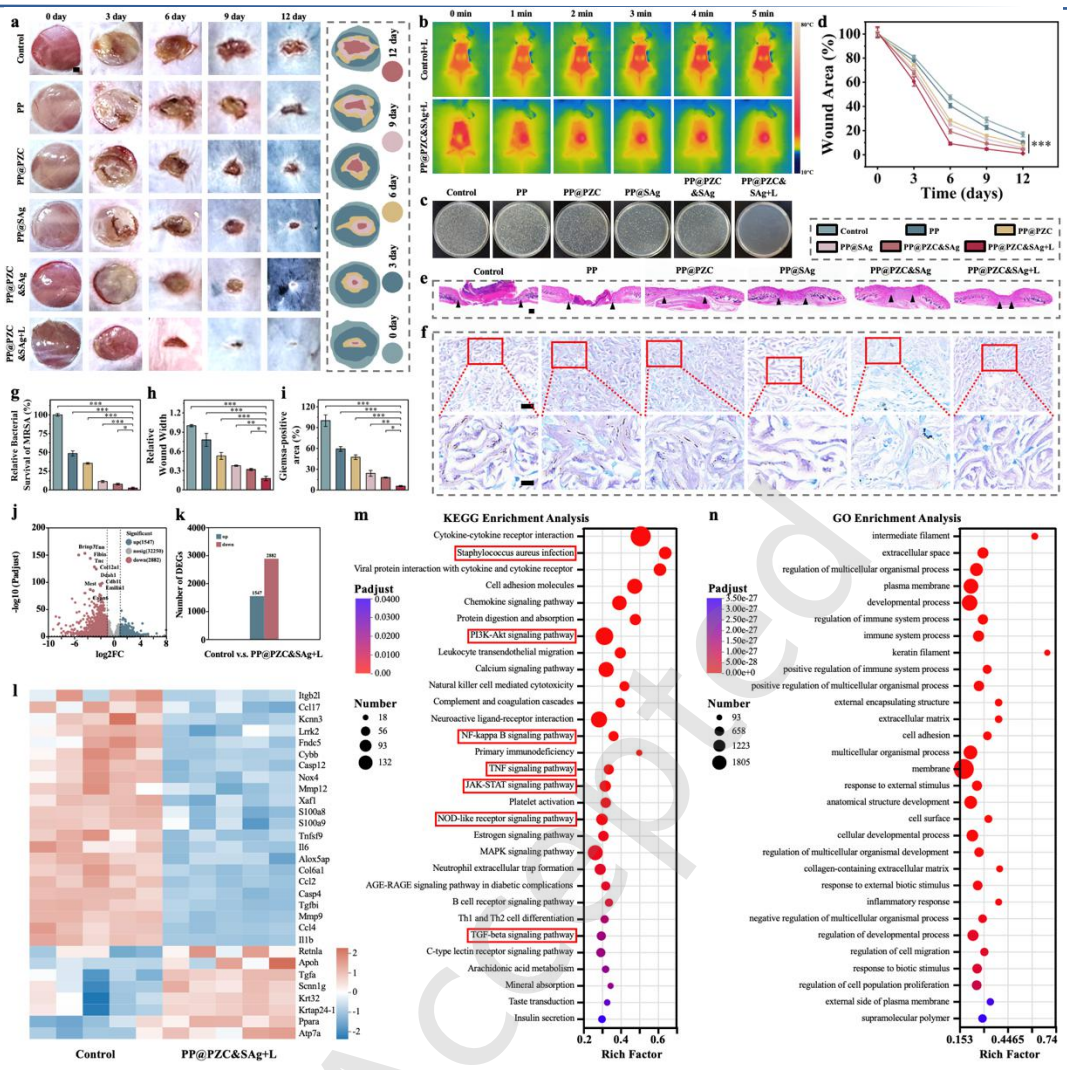

Figure 7 Hydrogels promote infected diabetic wound healing and wound sequencing analysis. (a) The ongoing process of wound healing (scale bar: 1 mm). (b) Temperature changes in the wound under laser irradiation. (c) The extent of bacterial infection at the wound site. (d) Statistical analysis of wound healing. (e) H&E staining of the wound (scale bar: 500 μm). (f) Giemsa staining of the wound (scale bars: 30 and 10 μm). (g) Quantitative analysis of bacterial infection in wounds. (h) Quantitative analysis of wound width on day 12. (i) Quantitative analysis of Giemsa staining. (j) Volcano plot of wound-associated DEGs. (k) Number of wound-associated DEGs. (l) Heatmap showing differences in the expression of specific genes in the wound. (m) Statistical enrichment of DEGs in the KEGG pathway. (n) GO enrichment analysis of DEGs.

In conjunction with wound sequencing results, we performed further histological observations. Masson's staining revealed that collagen content in hydrogel-treated wounds increased, with organized collagen fiber alignment, which was conducive to wound healing (Fig. 8(a) and 8(e)). Simultaneously, we performed immunohistochemical staining for IL-6 and TNF-α to assess the inflammatory status of the wound. The results showed that the expression levels of IL-6 and TNF-α were significantly reduced in the PP@PZC&SAg+L group, indicating an improved inflammatory status of the wound (Fig. 8(b), 8(c), 8(f), and 8(g)). *In vitro* experiments demonstrated that the hydrogels improved the tubule-forming capacity of HUVECs under HG conditions. We further investigated the effects of the hydrogels on angiogenesis *in vivo*. Immunofluorescence staining for α-smooth muscle actin (α-SMA) and platelet-endothelial cell adhesion molecule-1 (CD31) revealed extensive neovascularization in the PP@PZC&SAg+L group (Fig. 8(d) and 8(h)).

Furthermore, the aforementioned histological findings further indicate the hydrogel's potential to enhance healing quality and reduce scar formation. Compared with the control groups, the PP@PZC&SAg+L group showed a significant narrowing of the wound gap, indicating improved wound closure and early tissue remodeling. Masson staining showed that collagen deposition in this group was more ordered; an ordered collagen arrangement is a typical histological feature of a favorable scar outcome, whereas a disorganized, dense collagen structure indicates pathological scarring. At the same time, IL-6 and TNF-α levels were significantly reduced in this group, suggesting a timely resolution of inflammation, whereas persistent inflammation has been shown to be a major driver of fibrosis and hypertrophic scarring. Furthermore, α-SMA and CD31 staining revealed abundant neovascularization in this group; moderate angiogenesis is beneficial for tissue remodeling and scar reduction. Taken together, these histological findings indicate that the PP@PZC&SAg hydrogel accelerates wound closure and promotes improved healing quality and reduced scar formation.

We also conducted organ compatibility tests using mouse hearts, livers, spleens, lungs, and kidneys and verified the hematological compatibility of the hydrogel through hemolysis assays. As shown in Fig. S16(b) in the ESM and S17 in the ESM, the hydrogel exhibited good organ and blood compatibility. The mean hemolysis rates for each treatment group were 3.18 ± 0.34%, 3.55 ± 0.18%, 3.71 ± 0.21%, and 4.23 ± 0.23%, respectively. The hemolysis rates in all treatment groups were below 5%, meeting the application standards for biomaterials and demonstrating a high level of safety. To conduct a preliminary assessment of systemic exposure following the release of metal components from the hydrogel, we used ICP-MS to determine the concentrations of Ag, Zn, and Ce in the whole blood, as well as in the liver, spleen, and kidneys of mice on day 12 (Fig. S18 in the ESM). The results showed that the silver content in all whole blood samples was below the limit of quantification. Similarly, no quantifiable accumulation of Ag was observed in liver, spleen or kidney tissue. For Zn and Ce, there was no significant difference in concentration between the PP@PZC&SAg+L-treated group and the control group. This indicates that, on day 12, the hydrogel did not lead to systemic accumulation of these elements, thereby demonstrating its good safety profile. Finally, we evaluated the hemostatic properties of the hydrogels using a liver hemorrhage model and observed that hemorrhage in mouse livers was effectively inhibited by PCS and P(NIPAM-AM) (Fig. S19 in the ESM). This indicated that the hydrogel could help stop bleeding, reduce blood oozing, and stabilize the microenvironment at the wound site. Applying it to the wound helps promote early wound bed healing, thereby creating favorable conditions for subsequent cell proliferation and re-epithelialization.

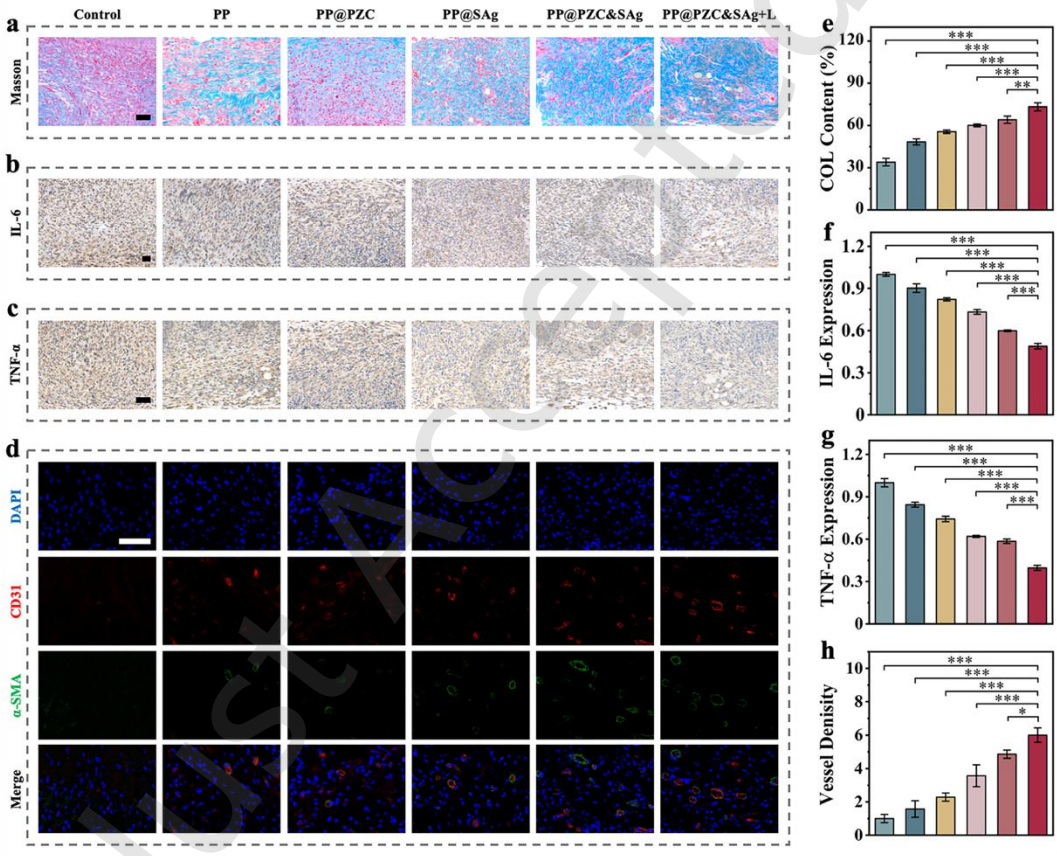

Figure 8 Wound immunohistochemistry. (a, e) Masson staining and quantitative analysis of diabetic wounds. (b, f) IL-6 staining and quantitative analysis of diabetic wounds. (c, g) TNF-α staining and quantitative analysis of diabetic wounds. (d, h) Immunofluorescence staining and quantitative analysis of α-SMA and CD31 in diabetic wounds. (scale bars: 50 μm).

3 Conclusions

In this study, we developed a novel ROS-responsive, bilayer, temperature-controlled hydrogel, PP@PZC&SAg. The lower layer of this bilayer hydrogel was loaded with PZC and in situ-synthesized Ag, enabling antibacterial, anti-inflammatory, and tissue-repair functions. In contrast, the temperature-sensitive properties of the upper hydrogel layer enabled temperature control. Macroscopic characterization confirmed that PP@PZC&SAg exhibited ROS responsiveness and could rapidly heat up to approximately 48.5 °C and remain stable. Antibacterial experiments demonstrated that PP@PZC&SAg hydrogels could effectively kill bacteria under near-infrared irradiation, induce cytoplasmic leakage in bacterial cells, and simultaneously disrupt bacterial biofilms, thereby exerting antibacterial effects through multiple mechanisms. Transcriptomic sequencing and related experimental results suggested that the antimicrobial activity of the hydrogel was associated with bacterial ATP production inhibition, membrane potential and metabolic process disruption, and oxidative stress induction. Cell-based experiments demonstrated that PP@PZC&SAg enhanced cell proliferation, migration, and tubule formation capacity, which were inhibited by high glucose levels. Finally, we validated the *in vivo* efficacy of PP@PZC&SAg using a diabetic wound infection model and found that PP@PZC&SAg significantly reduced bacterial infection at the wound site and accelerated wound healing. In summary, by combining thermosensitive hydrogels with photothermal effects and utilizing a bilayer hydrogel structure, we achieved safe and non-toxic antibacterial, antioxidant, and wound-healing effects, which have potential translational value for managing diabetic wounds.

4 Experimental

4.1 Materials

Chitosan, PVA, PBA–COOH, $AgNO_3$, $ZnCl_2$, $CeCl_3$, NaOH, PF127, NIPAM, AM, STZ, sodium citrate, and other analytical-grade chemical reagents were purchased from Macklin Biochemical Co., Ltd. (Shanghai, China). Reagents, antibodies, and assay kits used in the cell and histological experiments were obtained from Servicebio Technology Co., Ltd. (Wuhan, China). HUVECs were purchased from Procell (China). A commercial 2% mupirocin ointment (Bactroban®, GlaxoSmithKline) and a commercial hydrogel wound dressing (INTRASITE™ Gel, Smith+Nephew, UK) were used as clinically relevant benchmark treatments. Eight-week-old male C57BL/6 mice were purchased from Slauter Jinda Laboratory Animal Co., Ltd.

4.2 Bilayer hydrogel preparation

CSPBA was synthesized by grafting PBA-COOH onto chitosan (CS) [30]. CS was dissolved in 25 mL of 0.1 M MES, and the mixture was stirred for 2 h to obtain a 2% (w/v) CS solution. A solution containing 0.39 g of PBA-COOH, 0.77 g of 1-ethyl-3-(3-dimethylaminopropyl)carbodiimide, and 0.47 g of N-hydroxysuccinimide was prepared. The PBA-COOH solution was slowly added dropwise to the CS solution, and the mixture was maintained at pH 5.0–5.5 and stirred for 24 h. The mixture was dialyzed and freeze-dried to obtain CSPBA. CSPBA was dissolved in distilled water to a concentration of 2 wt%, and a 4 wt% PVA solution was prepared simultaneously. The two solutions were mixed in equal proportions and vortexed to obtain a PCS hydrogel. SS was extracted from silkworm cocoons. A mixture of 2 wt% CSPBA, 4 wt% PVA, 100 mmol/L $AgNO_3$, and 0.5% SS (w/v) was prepared and exposed to natural light for 24 h to promote Ag formation, ultimately yielding the PCS@SAg hydrogel. PZC synthesis was performed following previously reported methods [19]. A mixture of $ZnCl_2$ and $CeCl_3$ at a specific molar ratio was dissolved and added to an NaOH solution; after stirring for 4 h, a precipitate was obtained. ZnCe-LDO was obtained by heat treatment of the precipitate at 100 °C for 16 h. PZC was obtained by stirring ZnCe-LDO in a 10% (w/v) PF127 solution for 2 h. PZC was dissolved in CSPBA and mixed with PVA, $AgNO_3$, and SS according to the steps described above to obtain the PCS@PZC&SAg. The P(NIPAM-AM) hydrogel was synthesised according to previously reported methods [28]. The PP@PZC&SAg hydrogel was prepared by bonding PCS@PZC&SAg to P(NIPAM-AM).

4.3 Bilayer hydrogel characterization

Nanosilver was analyzed using a Hitachi U-3010 UV–visible spectrophotometer. XRD patterns were analyzed using a Rigaku SmartLab SE instrument, XPS spectra were analyzed using a Thermo Scientific K-Alpha instrument, and TEM images were analyzed using a FEI Talos F200x instrument. The thermoresponsive properties of the P(NIPAM-AM) hydrogel were evaluated by heating and cooling samples in sealed tubes and observing phase transitions. To assess ROS responsiveness, the PCS hydrogel was mixed with an H_2O_2 solution, inverted, and visually monitored for structural changes. A ZEISS Sigma 360 instrument was used for SEM imaging and elemental mapping of the composite hydrogel. FTIR spectra were measured using a Thermo Scientific instrument. The ^{1}H-NMR spectra of PCS and CS were recorded using a Bruker Avance 400 MHz NMR spectrometer with heavy water as the solvent. The rheological properties of the hydrogels were evaluated using a Haake Mars 40 rheometer. PCS@PZC&SAg was placed in PBS and H_2O_2 solutions, respectively, and the supernatants were collected at specific time points. The release levels of Ag, Zn and Ce were determined, and the cumulative release rates were calculated. SAg systems at varying concentrations were irradiated with an 808 nm laser at different power densities (0.5, 1.0, and 1.5 W cm^{-2}) for 10 min. During laser irradiation, temperatures were recorded in real time using an infrared thermal imaging camera. SAg samples at different concentrations were subjected to repeated on–off irradiation cycles using an 808 nm laser at 1.0 W cm^{-2}, and the results were recorded using an infrared camera. PP@PZC&SAg hydrogels containing different concentrations of SAg were subjected to repeated on–off irradiation cycles using an 808 nm laser at 1.0 W cm^{-2}, and the results were recorded using an infrared camera. The temperature-regulating properties of the composite hydrogel system were verified by irradiating it with an 808 nm laser at different power densities (0.5, 1.0, and 1.5 W cm^{-2}) for 10 min. The optical transmittance of P(NIPAM-AM)

hydrogels was measured at 808 nm at different temperatures using a Shimadzu 3600-plus.

4.4 *In vitro* antimicrobial testing

The antimicrobial properties were evaluated using *E. coli* and MRSA [31, 32]. The bacteria were co-cultured with hydrogels at 37 °C for 3 h; the Control+L and PP@PZC&SAg+L groups were initially irradiated with an 808 nm laser at 1.0 W cm^{-2} for 5 min. After 3 h, the bacterial suspension was spread onto solid Luria–Bertani (LB) medium and incubated in an inverted position for 15 h, followed by imaging of bacterial colonies. Following treatment, the bacteria were fixed in 2.5% glutaraldehyde and examined using TEM and SEM. Additionally, some precipitate was resuspended in PBS for SYTO-9 and propidium iodide staining, and live/dead images were captured. DCFH-DA staining was used to assess bacterial ROS levels. For biofilm analysis, MRSA was incubated in LB medium in 24-well plates. Hydrogel extracts from different groups were added, and the cultures were continued with or without laser irradiation. Photographs were taken, and the samples were examined 15 min after crystal violet staining. For quantitative analysis, the dye was dissolved in ethanol, and the optical density was measured at 570 nm. Similarly, biofilms were stained using a kit to distinguish between live and dead cells, and images were captured using confocal laser scanning microscopy (CLSM). ATPase and BCA protein assay kits were used to measure bacterial ATPase activity and protein levels, respectively, whereas the ONPG colorimetric assay was used to detect β-galactosidase leakage. Rhodamine 123 reagent was used to detect bacterial membrane potential, whereas SOD and POD kits were used to detect bacterial SOD and POD activities. The effect of antioxidants on the antibacterial activity of the hydrogels was assessed using GSH. After culturing MRSA in PBS and PP@PZC&SAg+L, bacterial pellets were collected by centrifugation and used for transcriptomic analysis. Each group was replicated three times.

4.5 Cell functional assays

Hydrogel extracts with different compositions were prepared and co-cultured with HUVECs in confocal culture dishes. Cell viability was assessed using a cytotoxicity assay kit, and images were captured using CLSM. The Ki67 immunofluorescence assay was used to assess cell proliferation. HUVECs were seeded in confocal culture dishes and co-cultured with hydrogel extracts in HG medium (125 mM glucose). Cells were fixed, permeabilized, blocked, and incubated with antibodies under appropriate conditions. After secondary antibody incubation, cell nuclei were stained with DAPI for 10 min and then observed. The EdU experiment further validated the proliferative capacity of cells. The migration-promoting ability of the composite hydrogel was validated using Transwell and scratch assays. Cells were seeded in six-well plates and treated with hydrogel extracts. A sterile pipette tip was used to scratch the cell monolayers. Cell migration was monitored and recorded at defined time points using optical microscopy. For angiogenesis analysis, Matrigel was evenly distributed in 24-well plates, and cells were seeded onto the Matrigel surface and co-cultured with hydrogel extracts. VEGF immunofluorescence staining was performed as previously described.

4.6 *In vivo* experiments

All animal experiments were approved by the Medical Laboratory Animal Science and Technology Ethics Committee of Air Force Medical University (20260028). A diabetic model was established in C57BL/6 mice (male; body weight, 25–30 g; 8 weeks old) by intraperitoneal injection of STZ. STZ was dissolved in 0.1 M sodium citrate buffer, and the injection dose was 50 mg kg^{-1}. Mice selected for subsequent experiments were those with stable fasting blood glucose levels ≥16.7 mmol L^{-1}, measured via tail vein sampling. Two symmetrical, 8-mm-diameter full-thickness skin wounds were created and simultaneously infected with MRSA, thereby establishing a mouse model of chronic wound infection. The mice were randomly divided into six groups: the control group, the hydrogel-only treatment group (PP), the composite hydrogel group containing only PZC (PP@PZC), the composite hydrogel group containing only SAg (PP@SAg), the composite hydrogel group containing both PZC and SAg (PP@PZC&SAg), and the composite hydrogel group receiving 1.0 W cm^{-2} laser irradiation (PP@PZC&SAg+L). Using PBS as the control, images were captured at fixed time points using a digital camera. On day 3, bacteria were collected and cultured to analyze the *in vivo* antibacterial activity of the hydrogel. Skin tissue was harvested from diabetic mice and fixed for subsequent experiments, including Giemsa and Gram staining, H&E and Masson's staining, IL-6 and TNF-α immunohistochemical staining, and α-SMA and CD31 immunofluorescence staining. Skin tissue samples were cryopreserved in liquid nitrogen for transcriptomic analysis. Select antibiotics and hydrogel dressings with representative clinical applications for *in vivo* controlled trials.

Fresh heparin-anticoagulated blood was collected from mice and centrifuged at high speed. PBS, H_2O, and hydrogel exudate were mixed with a diluted red blood cell suspension. After incubation for 1 h, hemolysis was observed, and the extent of hemolysis was assessed using a UV spectrophotometer. The hemolytic index was calculated using the following formula:

Hemolysis (%) = [(OD value of the experimental group − blank OD value) / (OD value of the control group − blank OD value)] × 100%

Visceral samples were collected from mice to assess organ compatibility. Whole blood, liver, spleen and kidney samples were collected from mice for analysis by inductively coupled plasma mass spectrometry (ICP-MS) to assess the accumulation of Ag, Zn and Ce *in vivo*. Finally, the hemostatic performance of the composite hydrogel was evaluated using a liver hemostasis assay.

4.7 Statistical analysis

Statistical analysis was performed using SPSS software (version 17.0). Data are expressed as the mean ± standard deviation (n ≥ 3). A two-tailed unpaired Student's t-test was used for comparisons between two groups, whereas one-way analysis of variance followed by Tukey's post hoc test was applied for multiple-group comparisons. Statistical

significance was defined as follows: * P < 0.05, ** P < 0.01, *** P < 0.001; ns, not significant.

Electronic Supplementary Material: Supplementary material (SEM images, rheological data, antimicrobial test results, cell culture results, etc.) is available in the onlineversion of this article at https://doi.org/10.26599/NR.2026.94909108.

Data availability

All data needed to support the conclusions in the paper are presented in the manuscript and the Electronic Supplementary Material. Additional data related to this paper may be requested from the corresponding author upon request.

Acknowledgements

This work is granted by the Funds of the Natural Science Foundation of Hangzhou (No. 2024SZRYBH180001) and the Key Laboratory of Artificial Organs and Computational Medicine of Zhejiang Province (No. SZD2025B003).

Declaration of competing interest

All the contributing authors report no conflict of interests in this work.

Author contribution statement

Songjie Li: Writing – original draft. Han Chen: Writing – review & editing. Xin Dan: Data curation. Pu Yang: Formal analysis. Yikun Ju: Conceptualization. Tong Li: Methodology. Yang Li: Resources. Lanjie Lei: Funding acquisition. Xing Fan: Supervision. All the authors have approved the final manuscript.

Informed consent

Not applicable

Ethics statement

All animal experiments were approved by the Medical Laboratory Animal Science and Technology Ethics Committee of Air Force Medical University (20260028).

Use of AI statement

None.

References

[1] Metwally, A. A.; Heydari, A. A.; McDuff, D.; Solot, A.; Esmaeilpour, Z.; Faranesh, A. Z.; Zhou, M.; Narayanswamy, G.; Xu, M. A.; Liu, X. et al. Insulin resistance prediction from wearables and routine blood biomarkers. *Nature* **2026**, *652*, 451-61.

[2] Liu, W.; Han, J.; Gong, W.; Zhang, F.; Cao, Q. Structure of pancreatic hIAPP fibrils derived from patients with type 2 diabetes. *Cell* **2026**, *189*, 1201-10.e10.

[3] Cho, H.; Lai, C. C.; Bonnavion, R.; Alnouri, M. W.; Wang, S.; Roquid, K. A.; Kawase, H.; Campos, D.; Chen, M.; Weinstein, L. S. et al. Endothelial insulin resistance induced by adrenomedullin mediates obesity-associated diabetes. *Science* **2025**, *387*, 674-82.

[4] Abizaid, A.; Mehran, R.; Oliva, A.; Chamié, D.; Staico, R.; Malik, F.; Vink, M.; Kurniadi, A.; Cao, D.; Capranzano, P. et al. Abluminus DES+ sirolimus-eluting stent versus everolimus-eluting stent in patients with diabetes and coronary artery disease (ABILITY Diabetes Global): results from a multicentre, randomised controlled trial. *Lancet* **2026**, *407*, 227-36.

[5] Zhang, Y.; Wen, D.; Ho, C.; Liu, Y.; Wang, X.; Zhou, Z.; Gao, Y.; Li, Q. HDAC5 deacetylates cytosolic ACTN4 during skin reepithelialization and represents a therapeutic target for chronic wound healing. *Sci. Transl. Med.* **2025**, *17*, eads0594.

[6] Wei, T.; Pan, T.; Peng, X.; Zhang, M.; Guo, R.; Guo, Y.; Mei, X.; Zhang, Y.; Qi, J.; Dong, F. et al. Janus liposozyme for the modulation of redox and immune homeostasis in infected diabetic wounds. *Nat. Nanotechnol.* **2024**, *19*, 1178-89.

[7] Xin, J.; Gao, L.; Zhang, W.; Song, X.; Yang, Y.; Li, W.; Zhou, X.; Zhang, H.; Wang, Z.; Wang, Z. et al. A thermogalvanic cell dressing for smart wound monitoring and accelerated healing. *Nat. Biomed. Eng.* **2026**, *10*, 80-93.

[8] Yang, Q.; Miao, Y.; Luo, J.; Li, C.; Li, X.; Chen, Y.; Wang, Y. Nanofibril-structured granular hydrogels harness stem cell retention and immunoregulation in diabetic microenvironment. *ACS Nano* **2025**, *19*, 6795-814.

[9] Arundel, C.; Mandefield, L.; Fairhurst, C.; Baird, K.; Gkekas, A.; Saramago, P.; Chetter, I. Negative pressure wound therapy versus usual care in patients with surgical wound healing by secondary intention in the UK (SWHSI-2): an open-label, multicentre, parallel-group, randomised controlled trial. *Lancet* **2025**, *405*, 1689-99.

[10] Zhao, S.; Lu, Z.; Cai, R.; Wang, H.; Gao, S.; Yang, C.; Zhang, Y.; Luo, B.; Zhang, W.; Yang, Y. et al. A wearable osmotic microneedle patch provides high-capacity sustained drug delivery in animal models. *Sci. Transl. Med.* **2024**, *16*, eadp3611.

[11] Tao, Z.; Li, Z.; Shao, Y.; Xiao, Y.; Fan, X.; Yang, L.; Sun, Z.; Cui, T.; Sun, Z.; Jiang, J. et al. Dynamically responsive hydrogel with mechanical stimulation enhances diabetic wound healing via activation of Piezo1-mediated efferocytosis. *Bioact. Mater.* **2026**, *60*, 607-25.

[12] Zhao, J.; Hu, Y.; Liu, C.; Yan, C.; Liu, Z.; Chen, Z.; Nie, Z.; Xu, X.; Cui, M.; Zhao, P. et al. Tissue-conforming organoselenium hydrogel with microphase-controlled acylhydrazone crosslinking kinetics expedites diabetic wound healing by inhibiting AGE-RAGE pathways. *Adv. Mater.* **2026**, *38*, e72776.

[13] Shi, R.; Hu, C.; Zhang, W.; Wan, L.; Shi, Y.; Zhen, N.; Mao, Z.; Zhou, B.; Luo, G.; Deng, J. Nanocascade engineering workshop for synergistic microenvironment reprogramming and EpSC revitalization in precise diabetic wound therapy. *Adv. Mater.* **2026**, *38*, e22987.

[14] Lu, P.; Ruan, D.; Huang, M.; Tian, M.; Zhu, K.; Gan, Z.; Xiao, Z. Harnessing the potential of hydrogels for advanced therapeutic applications: current achievements and future directions. *Signal Transduct. Target. Ther.* **2024**, *9*, 166.

[15] Xue, H.; Zhang, C.; Lin, D.; Gu, Q.; Sun, C.; Lin, X.; Zhang, C.; Lei, L.; Liu, L. Isoliquiritigenin micellar microneedle for pH monitoring and diabetic wound healing. *Mater. Today Bio* **2025**, *35*, 102356.

[16] Liao, P. Y.; Li, J. X.; Liu, J. C.; Xiong, Q.; Ruan, Z. Y.; Li, T.; Deng, W.; Jiang, S. D.; Jia, J. H.; Tong, M. L. Radical-induced photochromic silver(I) metal-organic frameworks: alternative topology, dynamic photoluminescence and efficient photothermal conversion modulated by anionic guests. *Angew. Chem. Int. Ed. Engl.* **2024**, *63*, e202401448.

[17] Li, J.; Zhang, Y.; Liu, Y.; Xu, Y.; Xu, H.; Ling, Q.; Tian, Z.; Ling, C.; Tang, Z.; Abdukahar, K. et al. Dual-action bisphosphonate hydrogel preserves cortical bone integrity and restores healing cascade in osteoporotic fracture-related infection. *Nat. Commun.* **2026**, *17*, 1276.

[18] Jin, H. G.; Zhao, P. C.; Qian, Y.; Xiao, J. D.; Chao, Z. S.; Jiang, H. L. Metal-organic frameworks for organic transformations by photocatalysis and photothermal catalysis. *Chem. Soc. Rev.* **2024**, *53*, 9378-418.

[19] Xiao, Y.; Xu, M.; Shi, Y.; Wang, J.; Li, Z.; Xiao, T.; Yu, H.; Lv, N.; Jiang, W.; Sun, Y. et al. ZnCe-LDO nanozyme-based multifunctional hydrogel promotes bone regeneration by inflammatory macrophage reprogramming and piezo1 activation. *ACS Nano* **2025**, *19*, 32606-28.

[20] Zhou, X.; Zhou, Q.; He, Z.; Xiao, Y.; Liu, Y.; Huang, Z.; Sun, Y.; Wang, J.; Zhao, Z.; Liu, X. et al. ROS balance autoregulating core-shell CeO_2@ZIF-8/Au nanoplatform for wound repair. *Nanomicro Lett.* **2024**, *16*, 156.

[21] Simoes de Jesus, D.; Buffonge, S.; Abis, G.; Buccafusca, R.; Baliga, R.; Warren, H. R.; Hobbs, A.; Ruppert, C.; Weiss, A.; Schermuly, R. T. et al. Zinc-mediated inhibition of soluble

epoxide hydrolase promotes pulmonary hypertension. *Am. J. Respir. Crit. Care Med.* **2025**, *211*, 1689-700.

[22] Li, H.; Wei, S.; Ling, Q.; Wang, R.; Liu, T.; Yu, H.; Zhao, P.; Zhang, K.; Bian, L.; Liao, W. Nanozyme-reinforced hydrogel spray as a reactive oxygen species-driven oxygenator to accelerate diabetic wound healing. *Adv. Mater.* **2025**, *37*, e2504829.

[23] Zhang, Z.; Yu, M.; Ma, C.; He, L.; He, X.; Yuan, B.; Zhang, L.; Zou, C.; Gao, Y.; Yang, H. A Janus smart window for temperature-adaptive radiative cooling and adjustable solar transmittance. *Nanomicro Lett.* **2025**, *17*, 233.

[24] Harimoto, T.; Jung, W. H.; Mooney, D. Delivering living medicines with biomaterials. *Nat. Rev. Mater.* **2025**, *10*, 191-210.

[25] Wei, X.; Buse, J. B.; Chen, H.; Desai, T. A.; Stevens, M. M.; Traverso, G.; Langer, R.; Gu, Z. Towards intelligent and miniaturized drug delivery devices. *Nature* **2026**, *651*, 897-908.

[26] Zhao, L.; Chen, S.; Chen, S.; Sun, Y.; Xi, L.; Huang, S.; Zhang, Y.; Dong, B.; Liao, Y.; Li, J. et al. Self-regulating hydrogel for diabetic wound healing: From animal models to a pilot clinical study. *Sci. Adv.* **2026**, *12*, eaed4981.

[27] Ma, P.; Liu, Y.; Yang, C.-y.; Yang, J.; Cao, Z.; Ren, B.; He, Z.; An, B.; Huang, C.; Liu, J. et al. A multifunctional bilayer hydrogel patch with photothermal-driven directional contraction and bioregulation for enhanced wound healing. *Mater. Today* **2025**, *90*, 297-313.

[28] Fu, H.; Xue, K.; Zhang, Y.; Xiao, M.; Wu, K.; Shi, L.; Zhu, C. Thermoresponsive hydrogel-enabled thermostatic photothermal therapy for enhanced healing of bacteria-infected wounds. *Adv. Sci.* **2023**, *10*, e2206865.

[29] Zhang, H.; Xu, H.; Luo, H.; Li, X.; Gao, T.; Wu, Q.; Zeng, D. A thermosensitive chitin hydrogel with mild photothermal-chemotherapy for facilitating multidrug-resistant bacteria infected wound healing. *Int. J. Biol. Macromol.* **2025**, *293*, 139428.

[30] Wang, J.; Liu, L.G.; Jiao, W. Q.; Yang, H.; Liu, J.; Liu, D. Phenylboronic acid-conjugated chitosan nanoparticles for high loading and efficient delivery of curcumin. *Carbohydr. Polym.* **2021**, *256*, 117497.

[31] Zheng, F.; Wan, X.; Zhang, Y.; Yue, Y.; Li, Q.; Zhang, Z.; Li, S.; Xu, H.; Su, Q.; Chen, X. et al. A multimodal defect-rich nanoreactor triggers sono-piezoelectric tandem catalysis and iron metabolism disruption for implant infections. *Sci. Adv.* **2025**, *11*, eads8694.

[32] Ni, Y.; Huang, Y.; Chen, Y.; Li, Y.; Liu, F.; Ji, J.; Jin, Q. An inhalable gallium-polyphenol nanoparticle blocks bacterial electron transport chain and signal transduction for anti-biofilm therapy. *Bioact. Mater.* **2026**, *57*, 1-15.

Electronic Supplementary Material

Bilayer hydrogel with ROS-triggered release and thermal regulation ability for diabetic infected wounds healing

Songjie Li[1], Han Chen[1], Xin Dan[1], Pu Yang[1], Yikun Ju[2], Tong Li[1], Yang Li[1] ✉, Lanjie Lei[3] ✉, and Xing Fan[1] ✉

[1] *Department of Plastic and Reconstructive Surgery, Xijing Hospital, Fourth Military Medical University, Xi'an 710032, China*
[2] *Department of Plastic and Aesthetic (Burn) Surgery, The Second Xiangya Hospital, Central South University, Changsha 410011, China*
[3] *Key Laboratory of Artificial Organs and Computational Medicine of Zhejiang Province, Shulan International Medical College, Institute of Translational Medicine, Zhejiang Shuren University, Hangzhou 310015, China*

✉ Address correspondence to Xing Fan, fanxing@fmmu.edu.cn; Lanjie Lei, leilanjie1988@163.com; Yang Li, liyangzx@fmmu.edu.cn

Supporting information to https://doi.org/10.26599/NR.2026.94909108

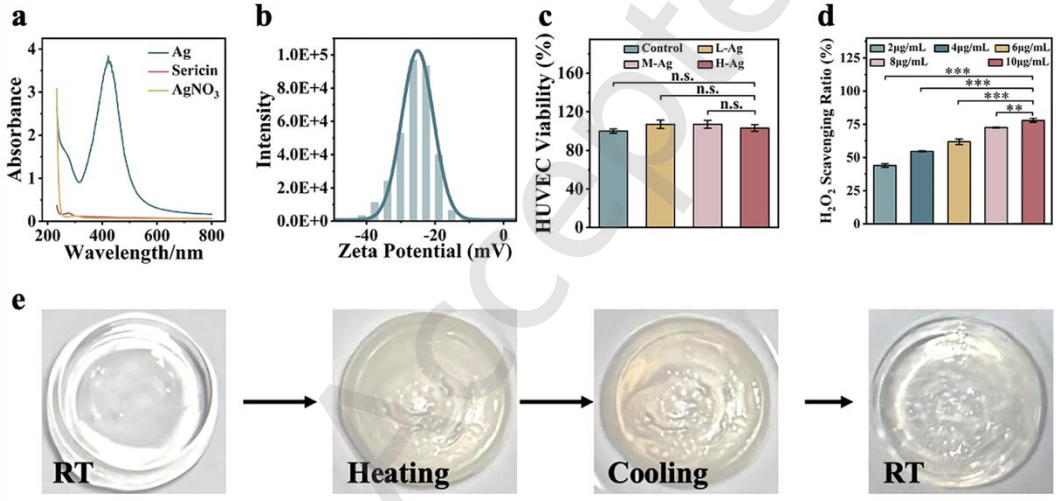

Figure S1 Characterization of nanoparticles and P(NIPAM-AM). (a) UV–vis absorption spectra of Ag nanoparticles, sericin solution, and $AgNO_3$. (b) Analysis of the zeta potential of Ag. (c) CCK-8 assay for Ag. (d) PZC's H_2O_2 scavenging experiment. (e) The thermosensitive properties of P(NIPAM-AM).

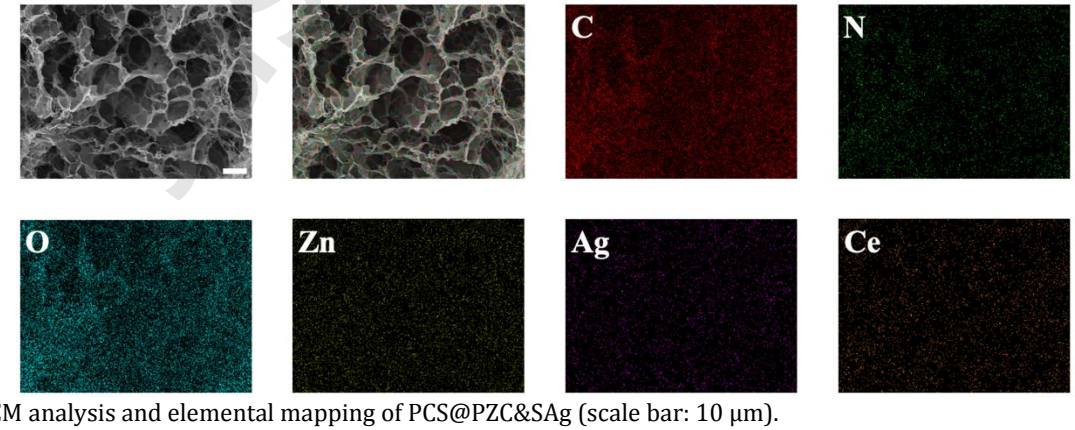

Figure S2 SEM analysis and elemental mapping of PCS@PZC&SAg (scale bar: 10 μm).

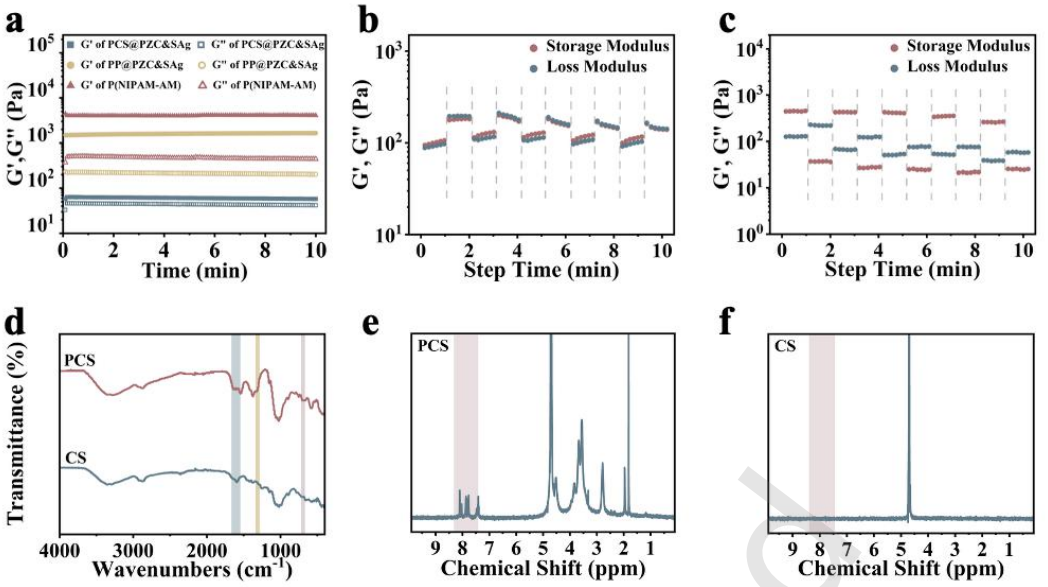

Figure S3 Characterization of hydrogels. (a) Rheological behavior of hydrogels under time scanning. (b) The rheological properties of PCS@PZC&SAg when the alternate step strain was switched from low to high. (c) The rheological properties of P(NIPAM-AM) when the alternate step strain was switched from low to high. (d) Fourier transform infrared spectroscopy analysis of PCS. (e) ^{1}H-NMR analysis of PCS. (f) ^{1}H-NMR analysis of CS.

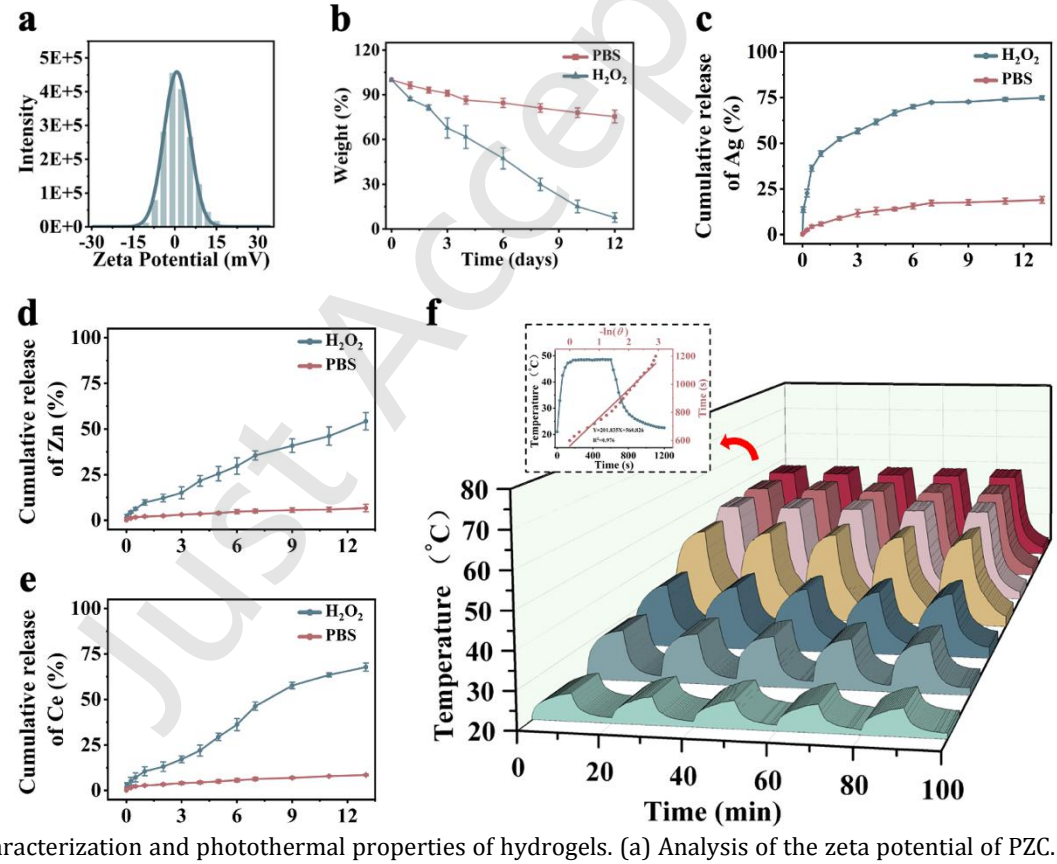

Figure S4 Characterization and photothermal properties of hydrogels. (a) Analysis of the zeta potential of PZC. (b) PCS *in vitro* degradation experiment. (c) Cumulative release curve for Ag. (d) Cumulative release curve for Zn. (e) Cumulative release curve for Ce. (f) Statistical analysis of the photothermal cycle of the PP@PZC&SAg.

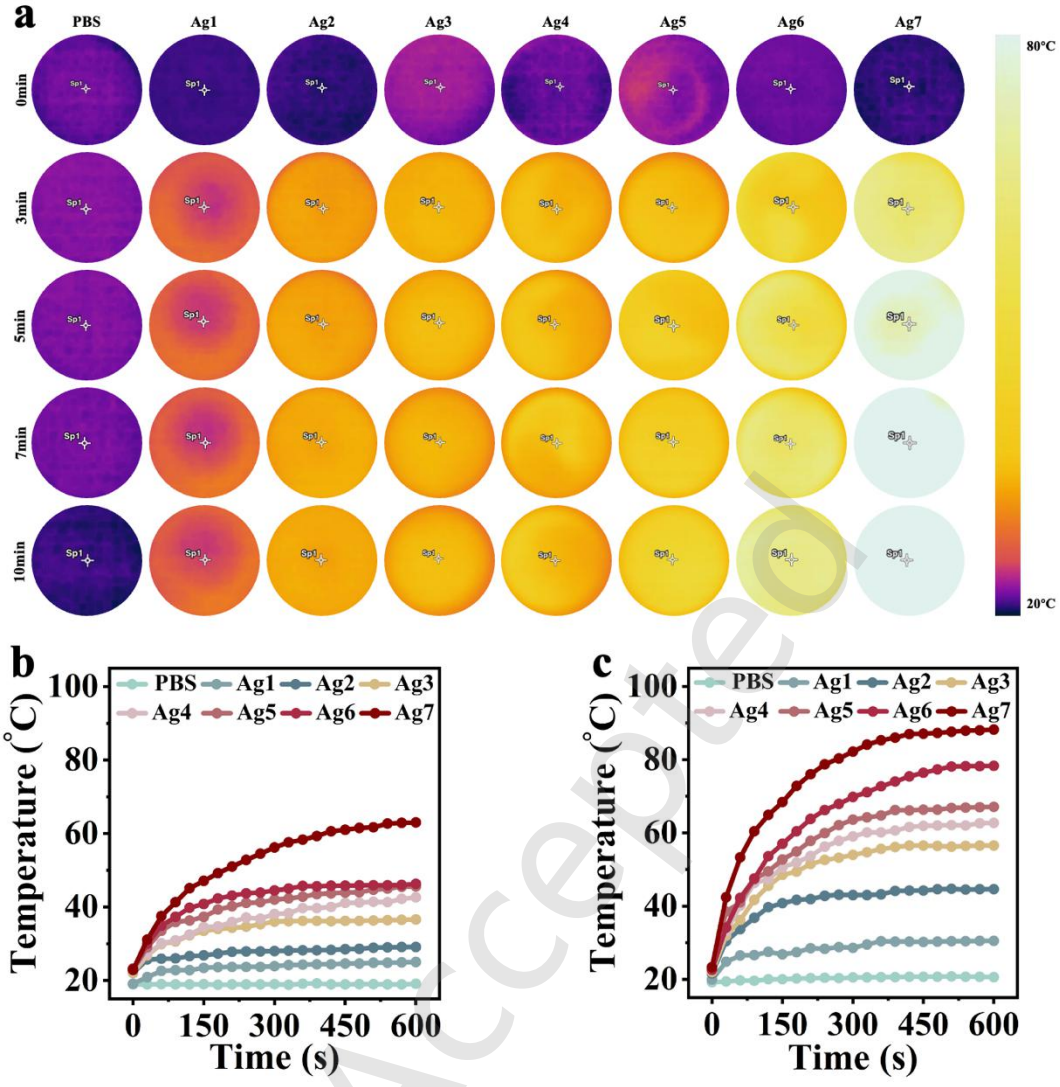

Figure S5 The photothermal effect of PCS@PZC&SAg at different power levels. (a) Temperature changes in PCS@PZC&SAg under laser irradiation at a power of 1.0 W cm^{-2}. (b) Statistics on temperature changes in PCS@PZC&SAg under laser irradiation at a power of 0.5 W cm^{-2}. (c) Statistics on temperature changes in PCS@PZC&SAg under laser irradiation at a power of 1.5 W cm^{-2}.

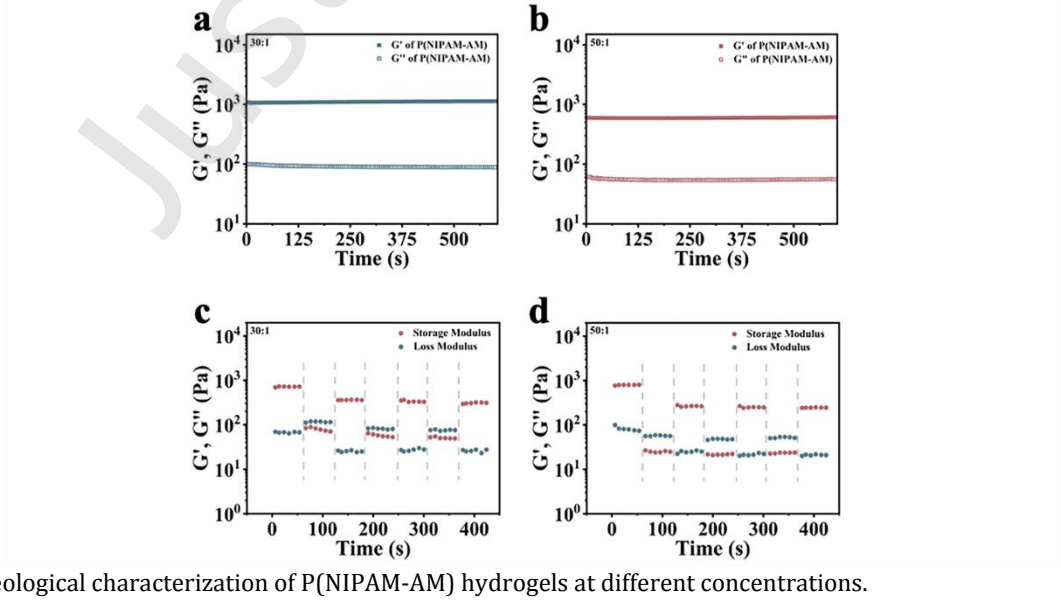

Figure S6 Rheological characterization of P(NIPAM-AM) hydrogels at different concentrations.

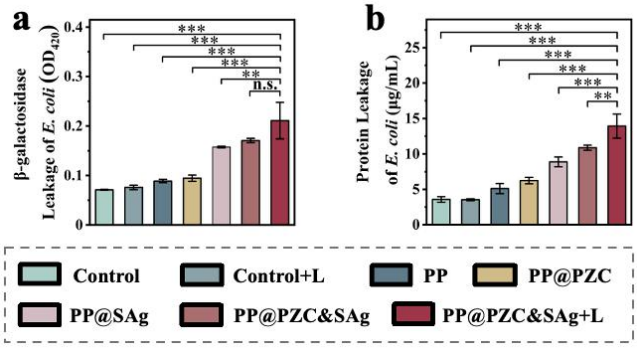

Figure S7 The leakage of *E. coli* bacterial contents.

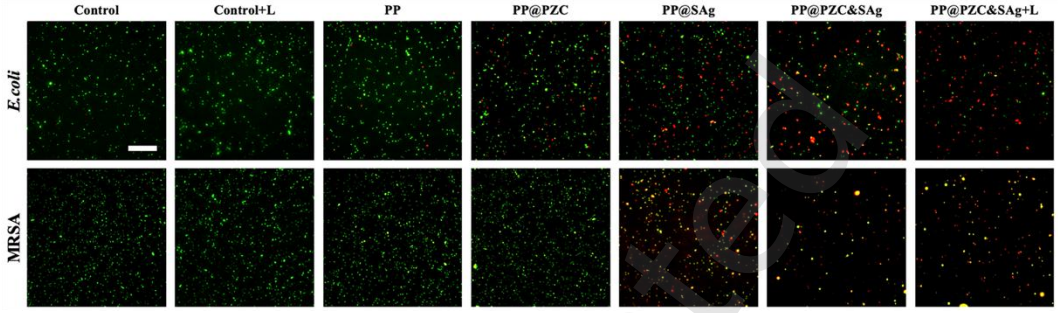

Figure S8 Live/dead staining experiment on bacteria (scale bar: 100 μm).

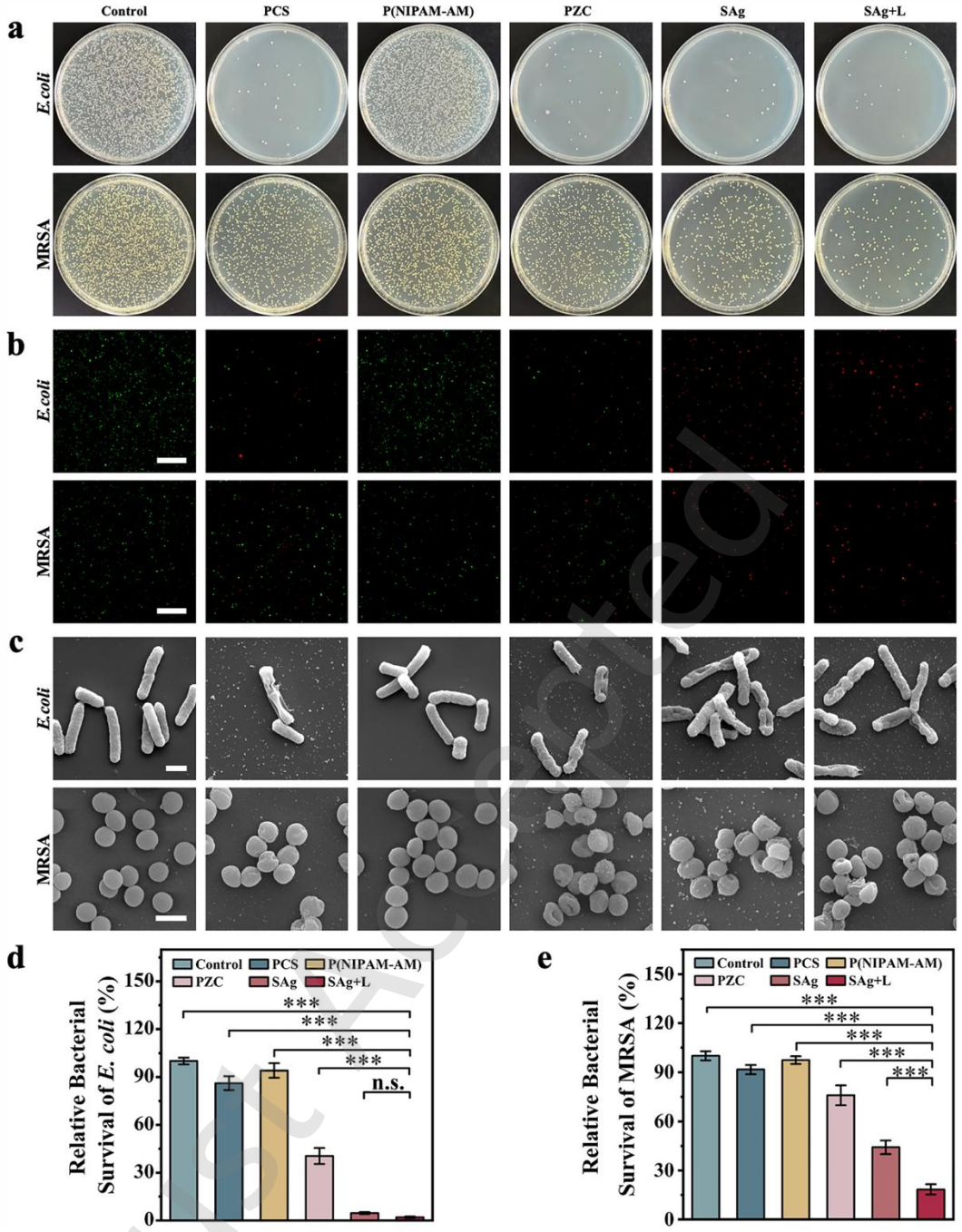

Figure S9 *In vitro* antimicrobial activity. (a, d, e) Bacterial plate count test and statistical analysis. (b) Live/dead staining experiment on bacteria (scale bar: 100 μm). (c) SEM observations of bacterial morphology (scale bar: 1 μm).

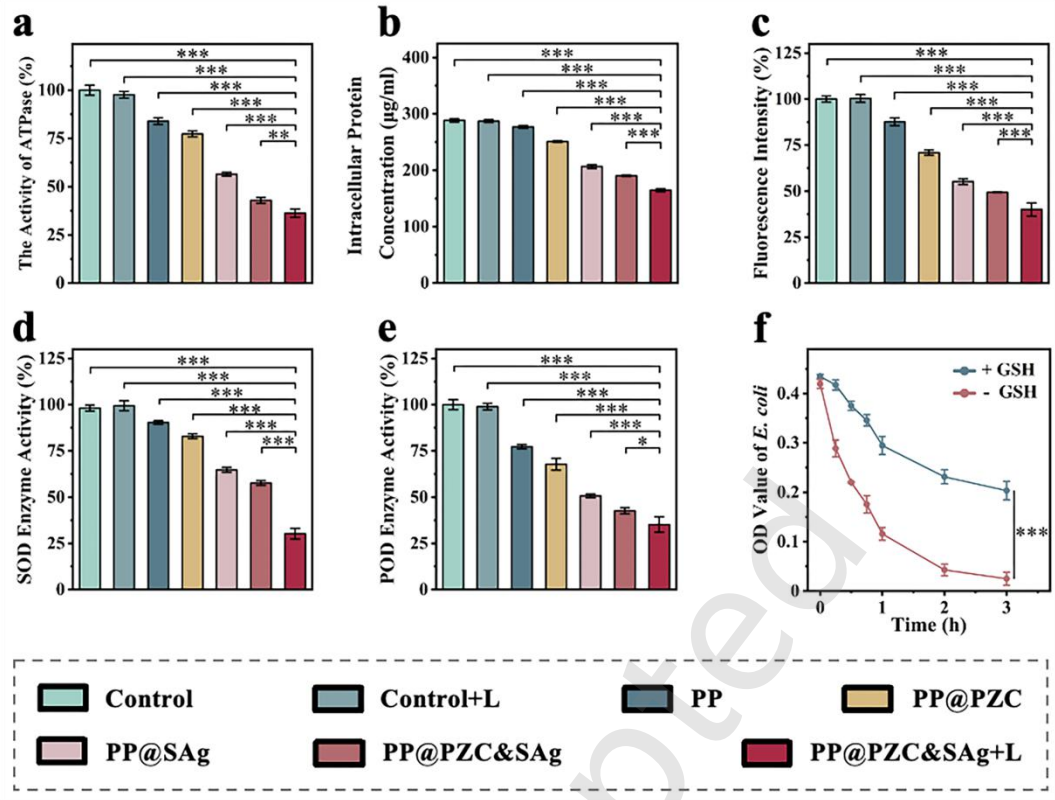

Figure S10 The antimicrobial activity of hydrogels against *E. coli*. (a) Hydrogels can inhibit the ATPase activity of *E. coli*. (b) Hydrogels can inhibit protein synthesis in *E. coli*. (c) Hydrogels can inhibit the membrane potential of *E. coli*. (d) Hydrogels can inhibit the SOD enzyme activity of *E. coli*. (e) Hydrogels can inhibit the POD enzyme activity of *E. coli*. (f) Bacterial relative survival rates with and without GSH.

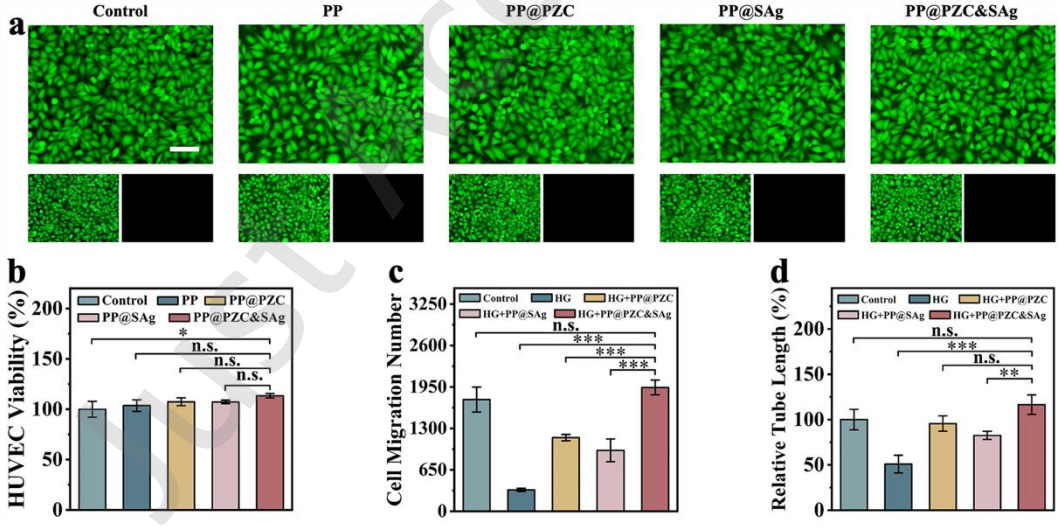

Figure S11 Experiments on the cellular functional aspects of hydrogels. (a) Cell live/dead assay (scale bar: 100 μm) and (b) statistical analysis. (c) Statistical analysis of Transwell experiments. (d) Statistical analysis of the tube formation assay.

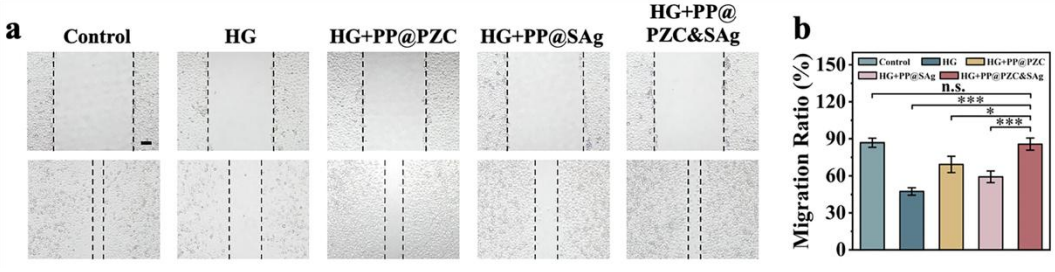

Figure S12 Cell scratch assay and statistical analysis (scale bar: 100 μm).

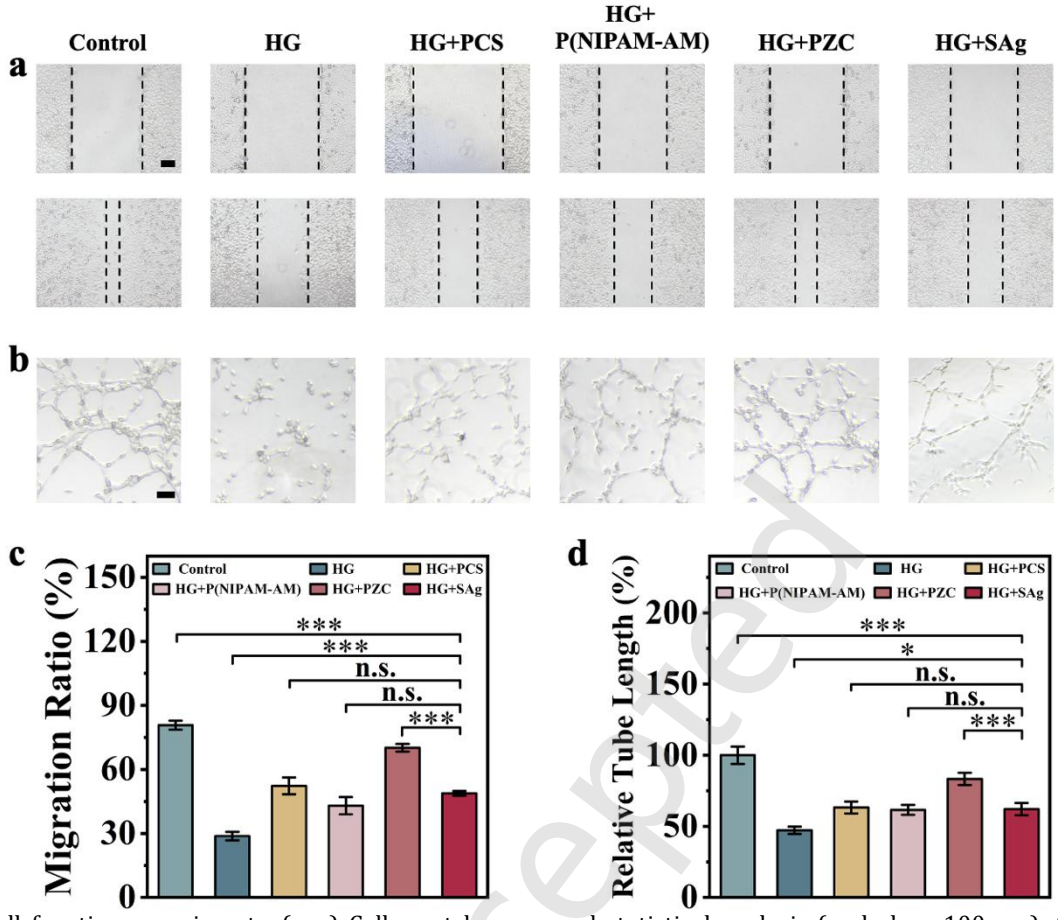

Figure S13 Cell function experiments. (a, c) Cell scratch assay and statistical analysis (scale bar: 100 μm). (b, d) Cell tube formation assay and statistical analysis (scale bar: 100 μm).

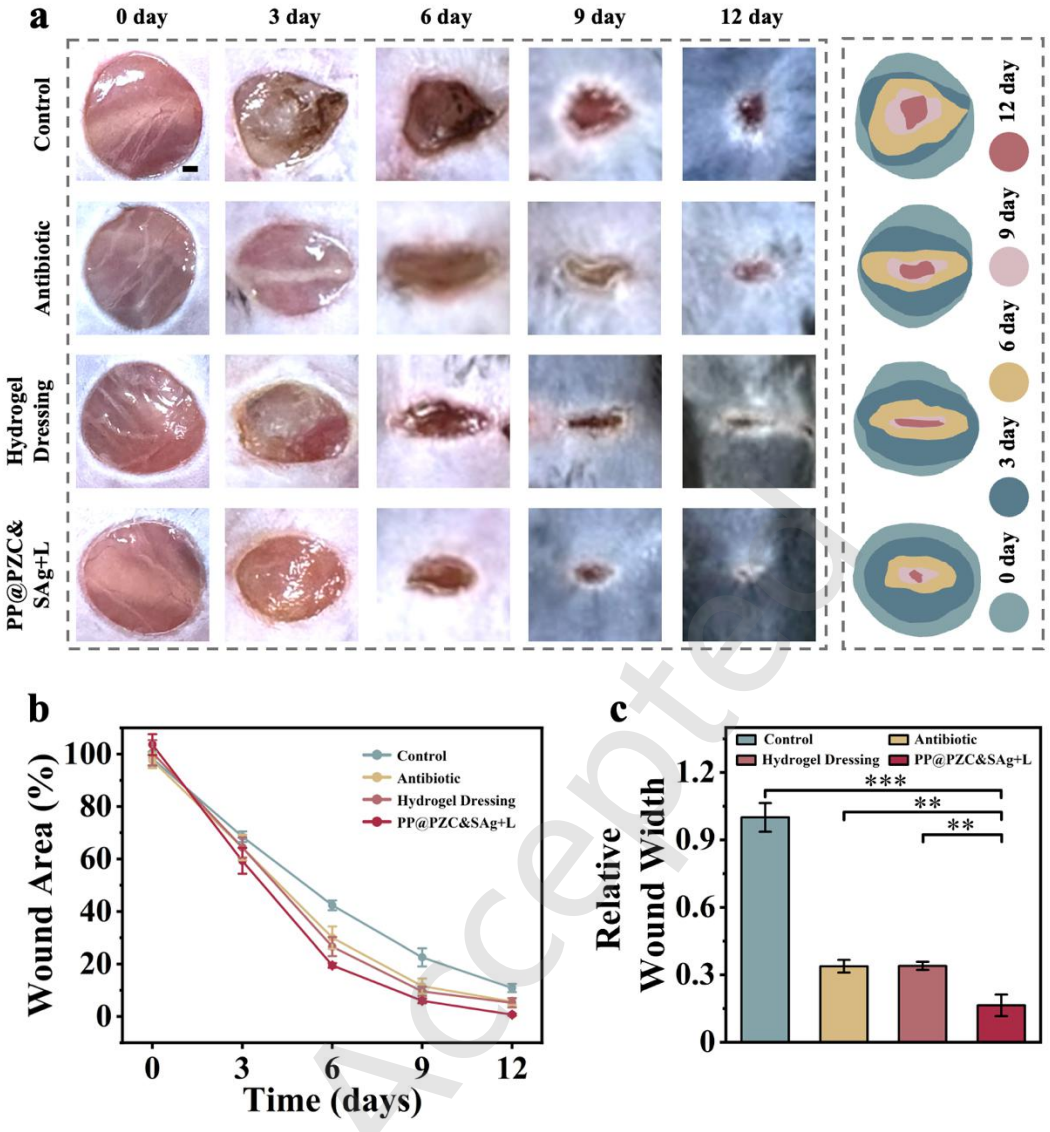

Figure S14 *In vivo* comparison of different wound treatments. (a) Continuous healing process of diabetic wounds under different treatments (scale bar: 1 mm). (b) Quantitative analysis of wound area over time. (c) Quantitative analysis of the relative wound width on day 12.

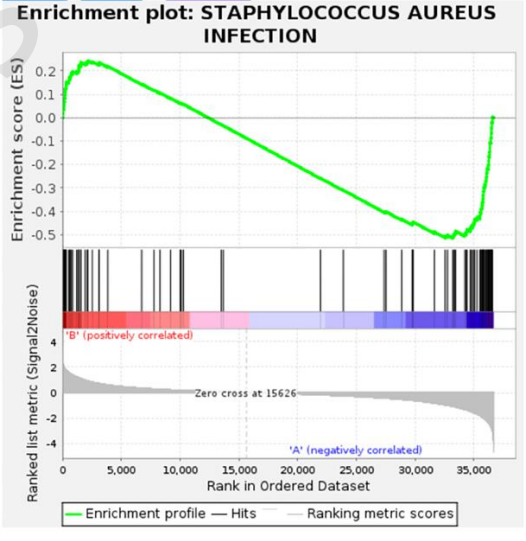

Figure S15 GSEA analysis of the *S. aureus* infection pathway.

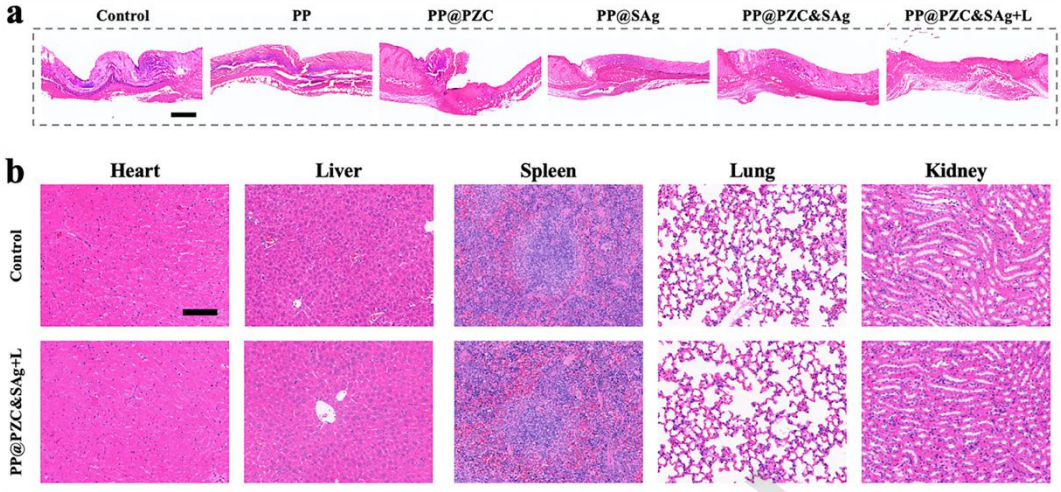

Figure S16 Histological analysis of animal wounds. (a) Gram staining of the wound site to assess bacterial infection (scale bar: 500 μm). (b) Organ compatibility of hydrogels (scale bar: 100 μm).

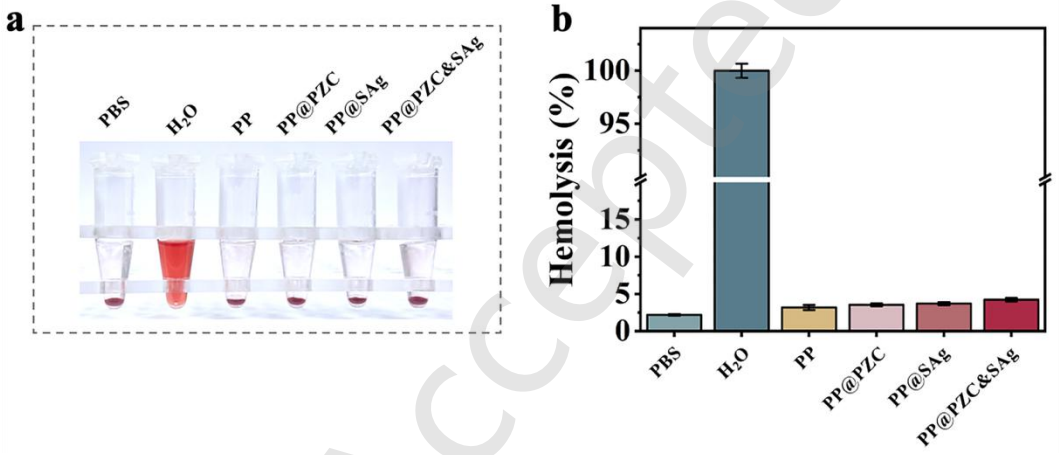

Figure S17 Blood compatibility of hydrogels and statistical analysis of the rate of hemolysis.

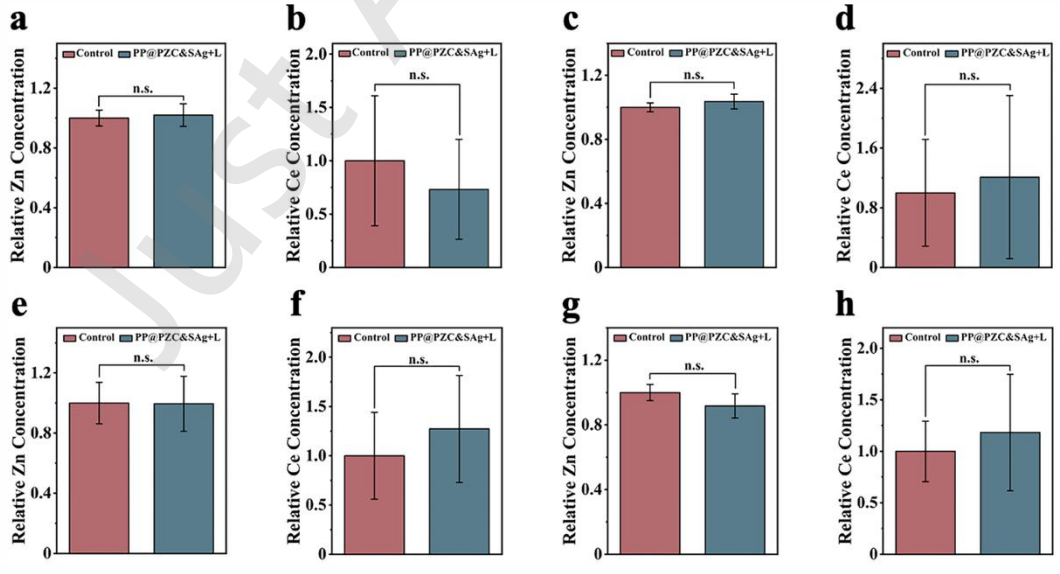

Figure S18 ICP-MS analysis of mice blood and tissues. Relative concentrations of Zn (a) and Ce (b) in mice whole blood. Relative concentrations of Zn (c) and Ce (d) in mice livers. Relative concentrations of Zn (e) and Ce (f) in mice spleens. Relative concentrations of Zn (g) and Ce (h) in mice kidneys.

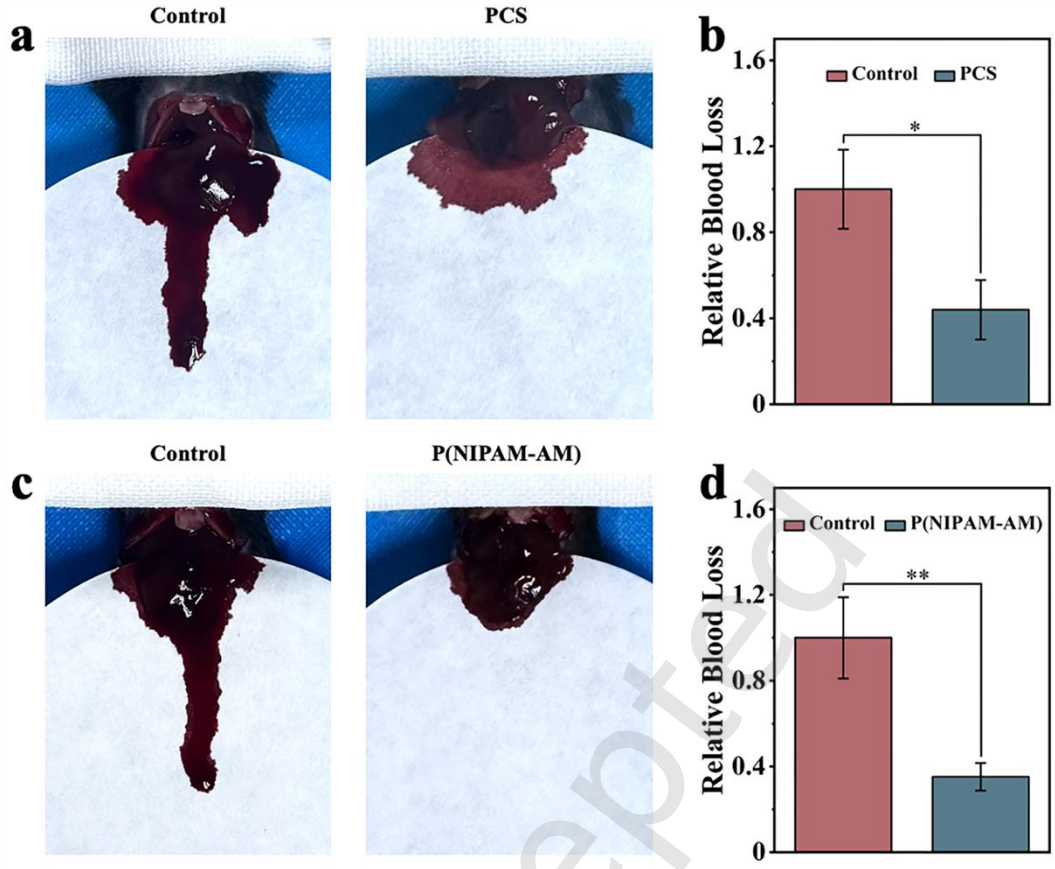

Figure S19 Liver haemostasis assay. (a) Experimental and (b) statistical analysis of hepatic haemostasis by PCS hydrogel. (c) Experimental and (d) statistical analysis of hepatic haemostasis by P(NIPAM-AM) hydrogel.

Address correspondence to Xing Fan, fanxing@fmmu.edu.cn; Lanjie Lei, leilanjie1988@163.com; Yang Li, liyangzx@fmmu.edu.cn